



ELSEVIER

Journal of Applied Geophysics 42 (1999) 169–228

JOURNAL OF  
APPLIED  
GEOPHYSICS

# Homeomorphic imaging approach — theory and practice

Boris Gelchinsky <sup>a,\*</sup>, Shemer Keydar <sup>b</sup>

<sup>a</sup> *Tel Aviv University, Department of Geophysics and Planetary Sciences, Ramat Aviv, Tel Aviv 69978, Israel*

<sup>b</sup> *The Geophysical Institute of Israel, PO Box 182, Lod, 71100, Israel*

---

## Abstract

The homeomorphic imaging (HI) approach is a generalization of the common mid-point (CMP) stack to media of arbitrary structures with the following key properties: it collects and enhances useful waves; no knowledge about the velocity structure of the overburden is required for correlation and stacking; and neither the resolution of nor the information about the target objects is degraded by stacking the data. The so-called common reflecting element (CRE) method, which has all three properties, was proposed by Gelchinsky [Gelchinsky, B., 1988. Common reflecting element (CRE) method. *Explor. Geophys.* 19, 71–75]. However, the CRE method did not only provide a generalization of the CMP method with the key properties; it also has a topological feature that led to the creation of the HI approach. Today, HI can be regarded as a system of methods and schemes for the study of seismic structures that are based on asymptotic wave theory and on fundamental topological ideas. HI is based on a single supposition: it assumes that a target wave exists on the chosen central trace. The next step makes use of the ensemble of all possible wave fronts that can be formed in the vicinity of the central ray corresponding to the chosen central trace. This approach is applicable to a medium of arbitrary structure without the assumption of a seismic model or its parameters. © 1999 Elsevier Science B.V. All rights reserved.

*Keywords:* Stacking; Homeomorphic images; Local time correction; Radius of curvature of the wave front; Angle of emergence; Inversion; Multifocusing

---

## 1. Introduction

In the 1960s, seismic exploration was thoroughly transformed, resulting in a significant increase of its efficiency. This transformation had two sources: the broad application of computers, and multifold data acquisition combined with the common mid-point (CMP) processing (Mayne, 1962, 1967; Dix, 1955; Hubral and Krey, 1980). Even today, these two features are key elements of seismic exploration. In many cases, the application of the CMP technique has striking results. Seismic sections which initially seem indecipherable become interpretable after CMP processing. Essentially, the CMP technique consists in a “stack” (a summation) of properly corrected traces.

Averaging (summation and stacking) of observed data is generally accompanied by a loss of information and resolution. Thus, one must find a stacking procedure that minimizes this reduction of

---

\* Corresponding author. Fax: +972-3-6409282; e-mail: shemer@gii.co.il

<sup>1</sup> Currently at: Geophysical Institute, University of Karlsruhe, Germany.

resolution of useful reflected waves. This means that all traces should be corrected before they are stacked in such a way that all target events are “in phase”. Thus, derivation of a reliable formula for time correction is crucial for any seismic stacking procedure.

The time correction used conventionally in reflection seismics was developed in two steps.

- First, the normal moveout (NMO) correction for *horizontally stratified* media was formulated (Dix, 1955). It formed the basis of the CMP technique.

- Next, the CMP time correction procedure was improved to allow for *dipping reflectors* in the dip moveout (DMO) method under the assumption of a known velocity model of the overburden (Levin, 1971; Sherwood et al., 1978; Yilmaz and Claerbout, 1980; Deregovsky and Rocca, 1981; Nottfors and Godfrey, 1987; Liner, 1990; Hale, 1991).

The DMO theory can be further improved by the use of overburden-velocity models of increasing complexity. However, it is very difficult to determine a velocity model of the overburden with sufficient accuracy, especially since the most interesting media are those with complex structure. Thus, one generally assumes relatively simple overburden models to derive time correction procedures. If such procedures are applied to data acquired over complex structures, a sub-optimum stack is to be expected.

Homeomorphic imaging (HI) is based on quite different concepts. There is only one assumption: the existence of a target event on the chosen central trace. This assumption — together with the geometry of a wavefront corresponding to selected set of source–receiver pairs — is sufficient to construct HI methods in such a way that they are applicable to arbitrary media without any a priori knowledge of the structure or physical properties. Each HI method may, therefore, be considered as a model-independent imaging method.

In the review of the HI approach presented here, the following aspects are discussed:

1. The basic concepts;
2. Different schemes of reflector mapping (“imaging”);
3. Methods of optimal correlation and stacking based on mapping schemes that produce five types of seismic sections;
4. Decomposition of these time sections into parts corresponding to different types of body waves, and the construction of a set (an “atlas”) of five types of homeomorphic images and a collection of the corresponding types of parameter curves for each wave;
5. An analysis of curves with the aim of finding their characteristic (critical) points and extracting geophysical and geological information;
6. Solutions of the kinematic inverse problem using parameter curves with distinct critical points as initial data;
7. Concepts which could form the basis of a combined interpretation of the atlas of images, the collections of curves, and the “true” kinematic seismic model in order to extract information concerning structure more efficiently than by conventional techniques.

The discussion of these items is accompanied by examples of application of HI methods to real data, acquired both on land and at sea.

We begin with an overview of the methods and procedures in their logical sequence in order to show that HI is a system of new methods applicable to a broad area of seismic data processing. It is not possible to fully develop the HI theory and technique in a single paper. Therefore, we confine ourselves to detailed descriptions of only a few of the basic HI methods, such as common reflecting element (CRE), common evolute element (CEE) and common shot point (CSP). Another basic HI method, *multifocusing*, is only briefly outlined, since its detailed description requires a special review; moreover, this issue already contains two papers devoted to multifocusing. A short sketch of a

solution to the kinematic inverse problem is mentioned and the common scattering-diffraction element (CSDE) technique is only touched. The problems connected with the general HI theory of time correction (including non-spherical approximation of wavefronts) and multiples are not included in this review.

## 2. Basic concepts and methods of the HI approach

The HI method was originally conceived as a generalization of the CMP method, which is based on simple overburden models. This generalization should be applicable to arbitrary structures, and it should satisfy three conditions:

- the method should be completely independent of an overburden model;
- the method should result in collecting and enhancing useful waves; and
- the summation of data should not degrade the resolution of the target objects.

A method which satisfied all three conditions, called the CRE method, was proposed by (Gelchinsky, 1988, 1989). It is based on a special type of mapping (imaging) of a reflector with the help of an associated wave front. A ray scheme illustrating CRE mapping is shown in Fig. 1.

It is assumed that a normally reflected target wave corresponding to the interface  $S$  exists on the chosen zero-offset trace  $u(A_0, A_0, t)$ . From this assumption, it follows that:

- there is a normally reflected ray  $A_0 \hat{C}_0 A_0$  corresponding to the trace  $u(A_0, A_0, t)$ .
- pairs of source  $A_k^+$  and receiver  $A_k^-$  ( $k = 0, 1, \dots, n$ ) can be located on a seismic line  $A_k^+ A_0 A_k^-$  in the vicinity of the central point  $A_0$  in such a way that the corresponding rays have a common reflecting point (CRP).

For an arbitrary two-dimensional (2D) structure and a set of source–receiver pairs, the pencil of rays has the form of the symbolic ray scheme in Fig. 1a. The term “symbolic” indicates that only the existence of such a scheme is required in the following.

A fictitious point source placed at the CRP (point  $C_0$  in Fig. 1b) would generate the same ray scheme. An associated fictitious wavefront  $\Sigma$  emitted by this source that reaches the central (“zero-offset”) point  $A_0$  at the moment  $t_0/2$  is also shown in Fig. 1b. The center of curvature of this wave front — located at point  $\hat{C}_0$  — is defined as a CRE image of the CRP. The image point  $\hat{C}_0$  and the fictitious front  $\Sigma$  are shown in the “image plane” in Fig. 1c.

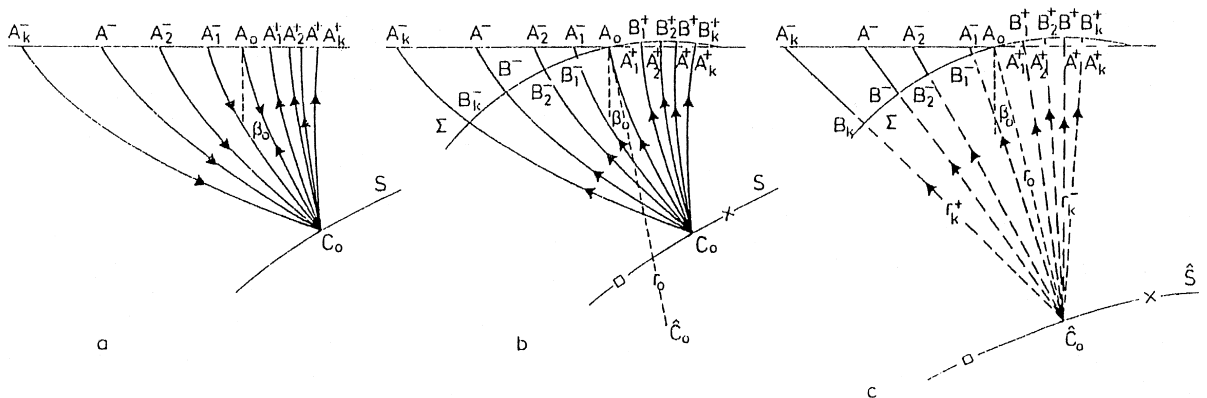


Fig. 1. Ray scheme for the CRE mapping. (a) Ray scheme corresponding to the CRE configuration of source–receiver pairs. (b) Ray scheme corresponding to a fictitious source located at the common reflecting point  $S$ . (c) Representation in the image plane of the fictitious front  $\Sigma$  and the CRE image  $\hat{S}$  of the reflector  $S$ .

By repeating this procedure for a set of center points, the CRE image of the reflector  $S$  as a locus of centers of curvatures of associated fronts emitted by a set of fictitious sources located on the interface  $S$  (Fig. 1c) is obtained. The box and the cross in Fig. 1b and c correspond to two different positions of the CRP (the image points) on the reflector  $S$  (with the CRE image  $\hat{S}$ ). For simplicity's sake, the corresponding central points and ray paths are not shown in Fig. 1b and c. It can be shown that the reflector  $S$  and its CRE image  $\hat{S}$  are locally “topologically equivalent”. This means that each point (or element) of the surface  $S$  corresponds to one point (or element) of the image. Following mathematical terminology, this image  $\hat{S}$  is called the “CRE homeomorphic image” of the object  $S$ , or simply the CRE homeomorphism (Gelchinsky, 1988, 1989).

In order to demonstrate the topological equivalence, we examine the HI image group (Keydar et al., 1990) which is simpler than the CRE image. Let us consider the point  $C_0$  (Fig. 1a and b) at which the central ray is normally reflected. From a physical point of view, this means that the point  $C_0$  is located on a smooth element commensurate with the Fresnel zone (Fig. 1a and b), and that Snell's law is valid. Furthermore, this implies that reflecting element is characterized not only by its position (coordinates), but also by its attitude (the direction of the normal). The reflecting element can be considered as an oriented (directed) element. The position is specified by horizontal and vertical coordinates  $\xi$  and  $\zeta$ , the direction of the normal specified by the angle  $\phi$  against the vertical. From this point of view, a reflecting interface is an ensemble of oriented elements. Now, we can emit a ray in the direction of the normal; the ray intersects the seismic line at a point  $A_0$  with coordinate  $x_0$ , arrival time  $t_0/2$  and angle of emergence  $\beta_0$  (Fig. 1b). This point exists because the existence of the reflecting ray connecting the point of reflection  $C_0$  and a point  $A_0$  on the seismic line is assured. There is only one connecting ray  $C_0A_0$  with the given arrival time making angles  $\phi$  and  $\beta_0$  at  $C_0$  and  $A_0$ , respectively, thus, the specular point  $C_0$  (the oriented element  $(\xi, \zeta; \phi_0)$ ) is uniquely mapped at point  $A_0$  (the image element  $(x_0, t_0/2; \beta_0)$ ).

From the coordinates  $x_0, t_0/2$  of  $A_0$  and the angle of emergence  $\beta_0$ , we can construct the coordinates  $\xi_0, \zeta_0$  of the point  $C_0$  by “back-propagating” the wave along the ray until the time becomes zero. The angle  $\phi_0$  is determined by the tangent direction to the ray at point  $C_0$ . There is only one ray which leaves point  $A_0$  under the angle  $\beta_0$  and reaches point  $C_0$  at moment  $t = 0$ . Thus, the image element  $(x_0, t_0/2; \beta_0)$  is uniquely mapped in the reflecting element  $(\xi_0, \zeta_0; \phi_0)$ , i.e., there is a one-to-one correspondence between the reflecting elements and the image elements. This means that the two elements are topologically equivalent. The local topological equivalence of elements implies the local topological equivalence of the *reflection surface* (carrier of oriented elements) and the *surface in the image space* specified by coordinates  $(\xi_0, \zeta_0; \phi_0)$ .

Two remarks are necessary: first, the object (or physical) plane and the image plane shown in Fig. 1b and c are, respectively, 2D subspaces of the corresponding 3D spaces. The reflector  $S$  and its image  $\hat{S}$  are the projections of the corresponding surfaces situated in these spaces. Strictly speaking, the topological equivalence has been proven only for the surfaces located in the respective 3D spaces; however, for simplicity's sake, we shall discuss the equivalence of the reflector  $S$  and its image  $\hat{S}$  located in the object and image planes, respectively. Secondly, the proof does not depend on any assumption regarding the structure of the medium. The only requirement is the existence of the normally reflected ray  $A_0C_0A_0$ , and that the field surrounding this ray is regular in the vicinity of the end point. The condition of regularity means essentially that the element of the associated (fictitious) wavefront is smooth.

We can now exploit an obvious property of the proposed mapping: the equality of time increments for the reflected and fictitious fronts corresponding to any source–receiver pair (Fig. 1a and b). The only difference between the two figures is that the ray direction on the left hand sides of the figures

are opposite. Therefore, the positions of the descending front and the fictitious front coincide at any point of the ray since the fronts are orthogonal to the same system of rays. The arrival times of fictitious and descending front at any point are generally different, but time *increments* for any pair of points (e.g.,  $A_k^-$  and  $B_k^-$ ) located on the same ray have equal magnitude and opposite sign. In particular, the left ascending part of the fictitious front  $\Sigma_0$  and the front descending and passing the central point  $A_0$  coincide, thus, the left side of front  $\Sigma$  actually consists of both an ascending and a descending front. The magnitudes and signs of the time increments for the right hand sides of the fictitious and reflected fronts in Fig. 1a and b are the same at any point of the rays  $C_0 A_k^+$  ( $k = 0, 1, 2, \dots$ ).

Let us assume as a first approximation that in the vicinity the seismic line  $A_k^+ A_0 A_k^-$  the velocity  $v_0$  is constant and the fictitious front  $\Sigma$  is spherical (Fig. 1c). Strictly speaking, the ray arcs ( $A_k^+ B_k^+$  and  $A_k^- B_k^-$ ) and the front  $\Sigma$  are the same in Fig. 1b and c. However, for a visual estimation of the degree of approximation, these arcs and the fronts are shown in Fig. 1c under the two assumptions (homogeneous velocity and spherical wave front). The ray arcs are straight segments and the front is a sphere with the radii (broken lines) emanating from the center  $\hat{C}_0$ . These radii are not rays because wave propagation in the image plane below the fictitious front is not considered in the HI approach.

Based on these assumptions, it is easy to derive the time correction formula (Gelchinsky, 1988; Rabbel et al., 1991; Steentoft and Rabbel, 1992):

$$\Delta\tau_k = \tau(A_k^+ C_0 A_k^-) - \tau(A_0 C_0 A_0) = A_k^+ B_k^+ / v_0 + A_k^- B_k^- / v_0 = \Delta\tau_k^+ + \Delta\tau_k^- \quad (1)$$

where  $\Delta\tau_k^+$  ( $\Delta\tau_k^-$ ) is the time correction corresponding to the  $k$ th receiver (source):

$$\Delta\tau_k^+ = \frac{\sqrt{r_0^2 + 2r_0 \sin \beta_0 \Delta x_k^+ + \Delta x_k^{+2}} - r_0}{2v_0} \quad (2)$$

$$\Delta\tau_k^- = \frac{\sqrt{r_0^2 + 2r_0 \sin \beta_0 \Delta x_k^- + \Delta x_k^{-2}} - r_0}{2v_0} \quad (3)$$

and

$$\Delta x_k^+ = A_k^+ A_0 = x^+ - x_0 \text{ and } \Delta x_k^- = A_k^- A_0 = x^- - x_0 \quad (4)$$

The  $x$ -axis is chosen to coincide with the seismic line. The positive  $x$ -axis makes the acute angle of entry/emergence  $\beta_0$  with the central ray  $C_0 A_0$  (or  $\hat{C}_0 A_0$ ). At the point  $A_0$ , the corresponding fictitious front  $\Sigma$  has the radius of curvature  $r_0$ , also called radius of normal incident point (Hubral, 1983). By using Snell's law, Gelchinsky (1988) demonstrated (see also Koren and Gelchinsky, 1989) that the offsets  $\Delta x_k^+$  and  $\Delta x_k^-$  of the  $k$ th source–receiver pair should be disposed along the seismic line according to:

$$\Delta x_k^+ = y_k + \alpha (y_k)^2, \quad \Delta x_k^- = -y_k + \alpha (y_k)^2 \quad (5)$$

with the coefficient  $\alpha$  determined by

$$\alpha = \sin \beta_0 / r_0 + 2 \cos \beta_0 Q'_0 / Q_0^{3/2} \quad (6)$$

where  $Q_0 = Q(\phi = 0)$  and  $Q'_0 = Q'(\phi = 0)$  are, respectively, the 2D spreading function and its derivative with respect to the radiation angle  $\phi$  at the CRP  $C_0$  calculated at the central point  $A_0$  (for the spreading function, see, for example, Cerveny and Ravindra, 1971 or Hubral, 1983; Cerveny,

1985, 1987; Tygel et al., 1992; Schleicher et al., 1993). The coefficient  $\alpha$  is called the “factor of asymmetry” (Gelchinsky, 1988).

Eq. (5) for the distance  $\Delta x_k^-$  from the central point to a source — respectively, for the distance  $\Delta x_k^+$  from the central point to a receiver — are expressed in terms of a parameter  $y$ . Any value of the parameter  $y$  determines the two offsets of a source–receiver pair.

If the maximum offset of a gather is relatively large, the spherical approximation of the wavefront and the straight-line approximation of the rays near the seismic line may not be admissible. This apparently vague statement can be given a precise meaning: an arc of the smooth 2D curve (element of front) can be developed successively into segments of (a) a straight line, (b) a circle (sphere), (c) a non-spherical line with a spherical evolute (a caustic), and so on. The velocity of a small region of the medium in the vicinity of the seismic (reference) line over the maximum offset (segment  $A_k^- A_k^+$  in Fig. 1) can be approximated by a sequence of structural models of increasing complexity. This sequence of structural models corresponds to the sequence of approximations of rays by “straight line segments”, “circular arcs”, “non-circular arcs”, etc. This means, in particular, that for a smooth front element and a medium with small variation of velocities near the seismic (reference) line, there is a specific offset interval corresponding to each approximation in the above sequence. Small offsets correspond to the approximation of rays by straight lines, moderate offsets to the approximation by circular arcs, large offsets to the approximation by non-circular arcs with a circular evolute, etc. The term “moderate distances” may justifiably be used in the HI theory with respect to circular approximation.

The offset interval for which approximation is valid can be determined in the following way. First, the formula for time correction corresponding to the *next higher* approximation should be obtained (e.g., the time correction formula for the non-spherical approximation of a front can be found in Gelchinsky and Keydar, 1993). Secondly, the parameters entering the expression for both approximations and the dominant frequencies should be known (or assumed to be known). Thirdly, the maximum admissible error should be defined, either as a fraction of the dominant period or in a more sophisticated way. The maximum offset for which the chosen approximation is valid can then be calculated.

The description of the CRE method presented here is more modern than that in Gelchinsky (1988). Initially, the aim was to create a method satisfying the three conditions stated above. It was assumed that there was only one generalization of the CDP concept, i.e., that to media of arbitrary structure. However, it was realized that the concept goes far beyond the generalization of the CMP method: investigation of the topological properties of the CRE lead to the creation of the HI approach. It is known in topology that a homeomorphism of a surface is not unique. Therefore, other mappings of a reflector into its HI image should exist. Several such mappings were subsequently developed.

Each type of HI is developed the same way: first, an associated front, orthogonal to a pencil of rays selected from a set of rays that corresponding to a special acquisition configuration is found. This associated front could be either a fictitious (as in CRE imaging, Fig. 1) or a real propagating front. Then an element of a target object is mapped into an element of the corresponding image with the help of the associated front. The image and the object should, as stated in the description of the CRE method, be topologically equivalent. This means that for the determination of a symbolic ray scheme similar to that shown in Fig. 1 only a central ray is required.

As a rule, the image is part of the caustic (or a locus of the point located on caustics) of the associated front. The parameters of the image are coordinates of source and receiver locations, arrival times, angles of emergence and entry, radius of curvature of the front at one of the end points and also the velocity close to this point. The time correction formula is then developed with the help of the ray

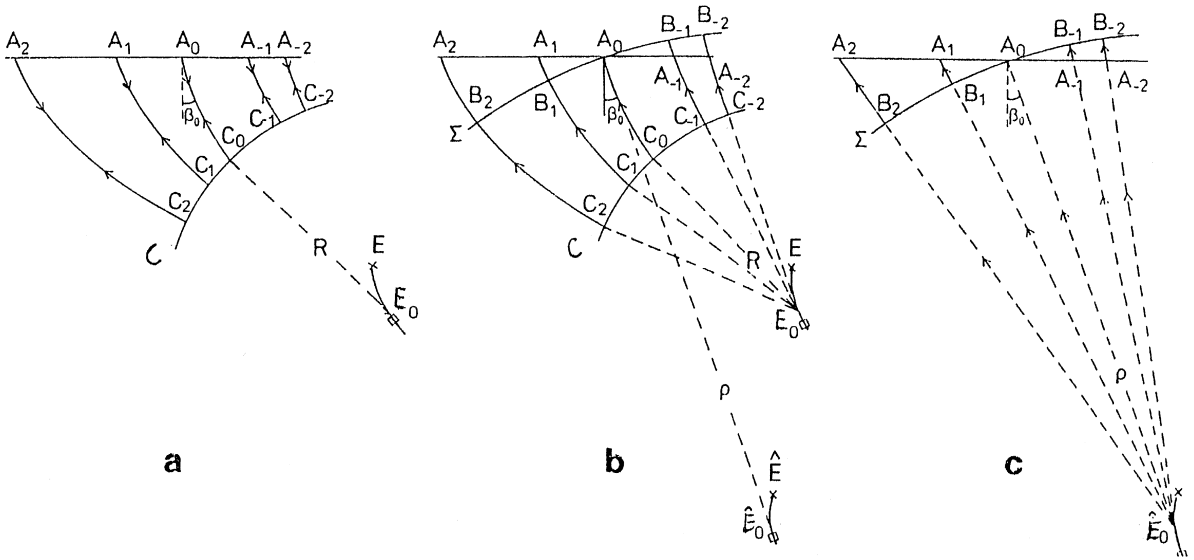


Fig. 2. Ray scheme for the CEE mapping. (a) Ray scheme corresponding to the CEE configuration of source–receiver pairs. (b) Ray scheme corresponding to the fictitious source  $\Sigma$  moving along the evolute  $E$  of the reflector  $S$ . (c) Representation in the image plane fictitious front  $\Sigma$  and the CEE image front  $\Sigma$  evolute  $E$ . Note that CEE front  $\Sigma$  shown here differs from the CRE front  $\Sigma$  depicted on Fig. 1.

scheme. Currently, there are the following HI methods: the common evolute element (CEE) method, the common source (receiver) point (CS(Rec)P) method, the combined HI and the common converting element (CCE) method (Gelchinsky, 1989; Keydar et al., 1990, 1993, 1996).

Below is a brief description of the CEE method. This method results, similar to the CRE method, in one of the main types of homeomorphic images (Fig. 2). In this method, a set of zero-offset traces is selected (Fig. 2a). A fictitious front orthogonal to a system of rays normal to the reflector  $S$  is found as follows: assume a fictitious source point on the evolute  $E$  of reflector  $C$  (Fig. 2b). The source moves along an element of  $E$  with the velocity of wave propagation. A source moving at such a velocity emits only one ray tangent to the evolute at each point. It follows from the property of the evolute that all emitted rays are normal to the reflector  $S$ . From another property of evolute follows that all rays reach the reflector at the same time equal to zero. The front  $\Sigma$  propagates upward into the overburden until at  $t = t_0/2$  it reaches the central point  $A_0$  of an array located along a seismic line  $A_{-2}A_0A_2$ . The position of front  $\Sigma$  is shown in Fig. 2b and c.

An element  $\hat{E}$  of the caustic of front  $\Sigma$  is defined as an image element of the evolute  $E$  (or an element of reflector  $C$ ). The central point  $\hat{E}_0$  of the image  $\hat{E}$  is the image point of the point  $E_0$  (or the point  $C_0$ ).

As in the CRE theory, one now uses the equality of time increments for the normally reflected and fictitious wavefronts. With the same approximation as in the CRE method (the spherical front and homogeneity of the velocity in the region near the CEE array), the time correction is derived as follows:

$$\begin{aligned} \Delta\tau_k &= \tau(A_k C_k A_k) - \tau(A_0 C_0 A_0) = 2[\tau(C_k A_k) - \tau(C_0 A_0)] = 2(B_k A_k)/v_0 \\ &= 2\left[\left(\rho_0^2 + 2\rho_0 \sin \beta_0 \Delta x_0 + (\Delta x_0)^2\right)^{1/2} - \rho_0\right]/v_0 \end{aligned} \quad (7)$$

Where

$$\Delta x_k = A_k A_0 = x_k - x_0 \quad (k = 1, 2, \dots, n) \quad (8)$$

$\rho_0$  is a radius of CEE front at the point  $A_0$  also called normal wave front (Hubral, 1983).

The CRE and CEE ray schemes are typical for most HI mappings. The ray schemes of other HI methods are constructed in a similar way. For the CSP method, mapping is associated with the real reflected front (Keydar et al., 1996). The mapping in the CCE technique is based on two fictitious fronts (for  $P$ - and  $S$ -waves, respectively) which produce two images  $\hat{P}$  and  $\hat{S}$  of the reflector (Gelchinsky, 1989). The combined HI method is accomplished in two stages: first, a CSP stack (with the CSP correction) is carried out, resulting in (quasi-) zero-offset traces and, secondly, the CEE stack is formed, generating the CEE image (Keydar et al., 1990).

### 3. Correlation and stacking procedures

The second stage of the HI approach is called ‘‘optimal correlation and stacking processing’’. In order to perform a stack of multifold data with the help of the time correction formula, one needs the HI parameters (the angles and radii), which are generally unknown. Algorithms for their determination and for stacking are described by Gelchinsky et al. (1985; 1986). The correlation procedure includes the following steps:

1. Selection of a signal model (wave impulse form) and a corresponding type of wavefield transform.
2. Selection of HI mapping(s), the corresponding types of source–receiver configuration and time correction formula.
3. Selection of a correlation criterion and a method of optimization.
4. Representation of a ‘‘possible region’’ in parameter space.

First, consider the selection of the signal model and wave transform. The following wavefield models are used.

(a) The simplest wavefield can be presented in the form:

$$u(x, t) = a(x, t - \tau(x))f(x, t - \tau(x)), \quad (9)$$

where  $\tau(x)$  is an arrival time at point  $M(x)$ ,

$$a(x, t) = \sqrt{(u(x, t))^2 + (V(x, t))^2}, \quad (10)$$

$$f(x, t) = \cos \varphi(x, t), \quad (11)$$

$$\varphi = \arccos(u(x, t)/a(x, t)), \quad (12)$$

and

$$V(x, t) = Hu(x, t) = \pi^{-1} P \int \frac{u(x, \tau)}{t - \tau} dt \quad (13)$$

is the Hilbert transform of the function  $u(x, t)$ . The symbol  $P$  indicates the principal value of the integral  $H(u)$ . The functions  $a(t)$ ,  $\varphi(t)$  and  $f(t)$  are called the *envelope*, the *instantaneous phase*, and the *normalized field* (normalized trace), respectively.

(b) A more general representation of the wavefield (Gelchinsky et al., 1985) is valid for complex situations and moderate distances:

$$u(x, t) = a[x, t - \tau_{\text{gr}}(x)] \cos \varphi[x, t - \tau_{\text{ph}}(x)], \quad (14)$$

where  $\tau_{\text{gr}}(x)$  and  $\tau_{\text{ph}}(x)$  are the group and phase arrival times at point  $M(x)$ .

(b) The most realistic representation of a wavefield formed as a result of complicated interference is given by (Gelchinsky et al., 1986):

$$u(x, t) = a[x, t - \tau_{\text{gr}}(x)] \cos \varphi[x, t - \tau_{\text{ph}}(x)], \quad (15)$$

where

$$\varphi(x, t) = \Phi[x, t - \tau_{\text{gr}}(x)] + \varpi_0[t - \tau_{\text{ph}}(x)], \quad (16)$$

and  $\Phi(x, t)$  is a slowly varying component of the instantaneous phase  $\varphi$  depending on group properties of the wavefield. It is useful to note that, from a general point of view, the group component  $\Phi(x, t)$  is always present in the phase  $\varphi$ . It can be neglected in correlation, provided the array aperture is relatively small and the value of  $\Phi$  does not change over the aperture.

As the conventional time correction, HI time correction based on the approximate description of wave kinematics by the rays. The corresponding wave form is given by Eq. (9). In this case, the instantaneous phase depends only on the kinematic attributes. If a wave package (Eqs. (15) and (16)) is correlated, the instantaneous phase has a slowly varying term depending on the group travel time, which can be considered as a kinematic attribute of a wave package. Therefore, in the kinematic stage of data processing the normalized wavefield  $f(x, t) = u(x, t)/a(x, t)$  is used to search for optimal parameters. The amplitude envelope  $a(x, t)$  is used in the calculation of optimally stacked wavefield.

The next step of optimal processing — selection of a criterion of correlation and an optimization procedure — is a special problem requiring detailed consideration (see Gelchinsky et al., 1985, 1986). Many of the criteria described in these papers can be used in HI processing; so far, only the semblance (Student's criterion) has been applied in some practical tests with the simplest signal model. The use of the third signal model and the criterion of combined group–phase correlation would be a crucial point in the HI method of determining subsurface angle points in the image plane (Gelchinsky et al., 1995).

A flow-chart for the optimal correlation program is shown in Fig. 3. A set of traces recorded by multifold coverage is stored together with the acquisition parameters (Blocks 1 and 2). The equations for time correction and space distribution corresponding to a chosen HI method is selected (Block 3), then the data are represented by grid values of a parametric mesh (Block 4).

Before beginning a search for the optimal correlation and stack, some preliminary operations are carried out. The traces stored in Block 1 are normalized, and the envelopes are formed (Block 5). A central point  $x_0$  is selected, and a set  $P_1$  of parameters is chosen (Block 4). Included in  $P_1$  are an angle  $\beta_0$  and a radius ( $r_{\text{cre}}$  or  $r_{\text{cee}}$  or  $r_{\text{csp}}$ ). HI gathers are formed by attaching the parameters to the appropriate traces (Block 6). The selected traces are corrected (Block 7) using the equations stored in Block 3. The correlation criterion  $W$  is determined for the corrected gather for each instant  $t_0$  (Block 8). The criterion trace  $W(x_0, t_0; P_1)$  is stored temporarily (Block 8). This process is repeated  $Q$  times with parameter sets  $P_2, P_3, \dots, P_Q$ , resulting in a set of traces  $W(x_0, t_0; P_q)$  ( $q = 1, \dots, Q$ ). Finally, the optimum set of parameters for the position  $x_0$  and for each instance  $t_0$  is determined by locating the maximum of the criterion  $\hat{W}(x_0, t_0; \hat{P}(x_0, t_0))$ . It should be noted that this is the simplest optimization scheme. It is reliable, though time consuming. In practice, different optimization methods from the scientific literature or from computer packages are used.

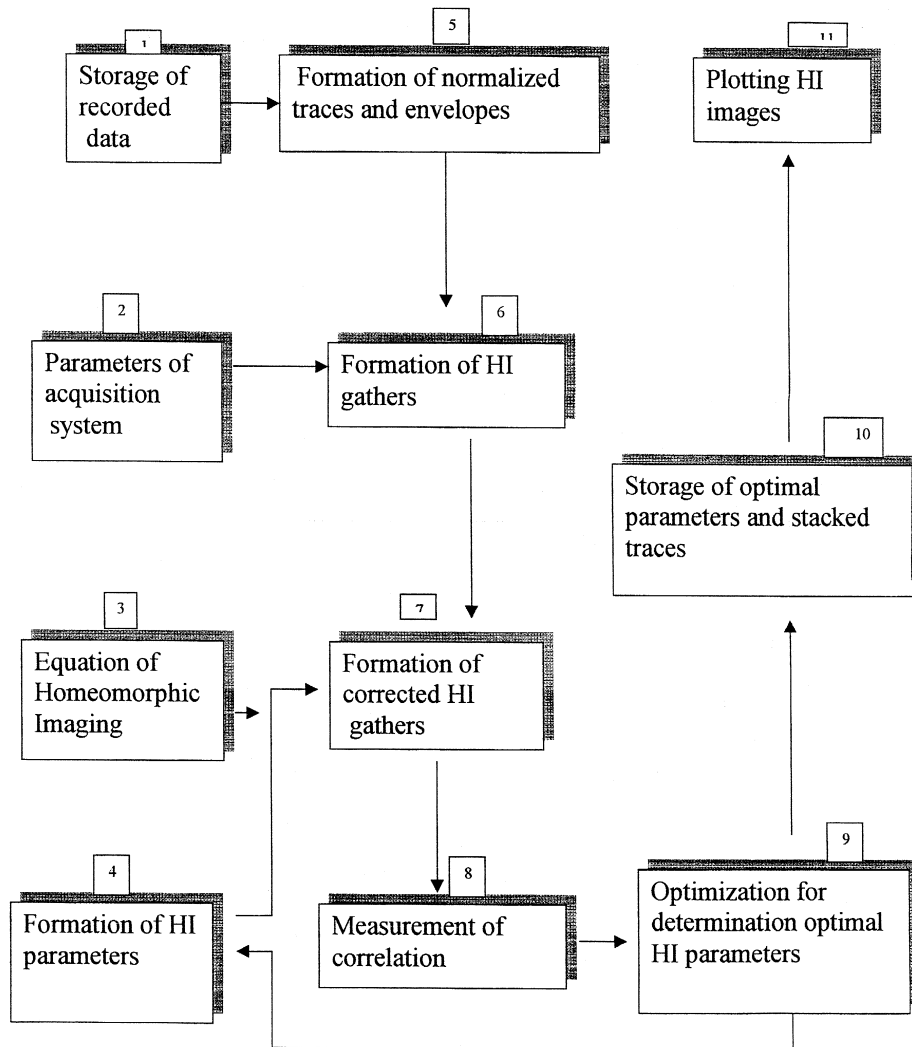


Fig. 3. Flow chart of the correlation-stacking procedure.

Once the optimization process has been completed at a given central point, the field is stacked using the optimal parameters. Each type of HI method stacks the data with a specific distribution and a specific time correction. The resulting trace can be regarded as a wavefield reflected from an interface at an image point that corresponds to the type of HI stack. This interpretation makes sense only in the kinematic context, therefore, this type of stack should properly be called “quasi-focusing”. For convenience, however, we shall refer to it as focusing. These cycles are repeated for different central points, resulting in four types of time section. Each time section is a 2D function of coordinates  $x$  and  $t$  of a central point.

The four time sections are:

- (a) a time section  $\hat{u}(x,t)$  representing an optimally stacked wavefield;
- (b) a semblancegram  $S(x,t)$  presenting maximum values of semblance at point  $x$  and time  $t$ ;
- (c) an anglegram  $\beta(x,t)$  representing the angle of emergence/entry; and

(d) a radiusgram  $r_{cre}$  (or  $r_{cee}$  or  $r_{csp}$ ) presenting the curvature of the wavefront associated with the method used.

In view of the results of the multifocusing technique, only two of the three radiusgrams listed under (d) are independent. The radiusgram of the third type could be used to verify the consistency of the data.

#### 4. Decomposition procedure, parameter curves and critical points

The next step of HI processing is the decomposition of the time sections into parts corresponding to different body waves, the construction of a set of their homeomorphic images (called an “atlas”), and collection of the parameter curves for each body. The following step is a curve analysis with the aim of locating the critical points. These steps are not purely theoretical, but include some procedures that are not completely formalized. They are, therefore, selected differently from before. These stages of HI processing are presented by examining results of HI correlation to synthetic and/or real data. The presentation starts with a simple synthetic example for which it is not necessary to apply the decomposition procedure. The decomposition procedure is examined later on by considering more complicated examples.

The first example shows the application of the HI correlation technique to the simple synthetic two-layered model of Fig. 4. The zero-offset seismogram (time section), angles of entry and radii of curvature of the CEE front reflected from the first interface (Fig. 5b,c) and the second interface (Fig. 7a,b) were calculated with the ray geometric approximation. CEE processing with unknown velocities was applied to the calculated seismograms. The CEE stacked section is shown in Fig. 6a. The angles of entry and radii of curvature obtained by CEE processing for the first reflector are shown in Fig. 6b,c and for the second reflector in Fig. 8a,b. A useful characteristic of the time sections obtained in simple models as that of Fig. 4 is that the fields of different reflected waves are separated, therefore, application of the decomposition procedure of time sections is unnecessary. We can, thus, compare the results of calculation and processing related to the angle or radius curves directly without resorting to the decomposition procedure.

The calculated zero-offset section (Fig. 5a) and the stacked CEE section (Fig. 6a) very close, almost the same. The angle (radius) curves for the first reflector, calculated and estimated by CEE processing virtually coincide, i.e., the estimates of the angles of entry and CEE radius based on the optimal correlation procedure are very accurate. For such simple models, the anglegram and radiusgram practically coincide with the angle curve and radius curve, respectively.

An important feature of these parameter curves is the presence of characteristic (critical) points. For example, there are five critical points on the angle curve (Figs. 5b and 6b). The leftmost point

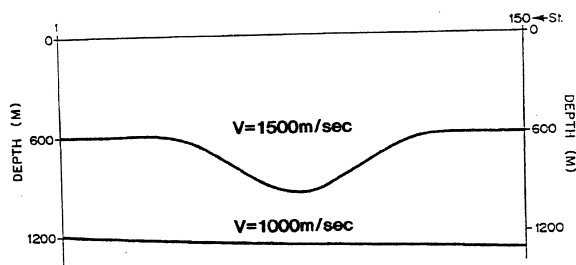


Fig. 4. Two-layer model.

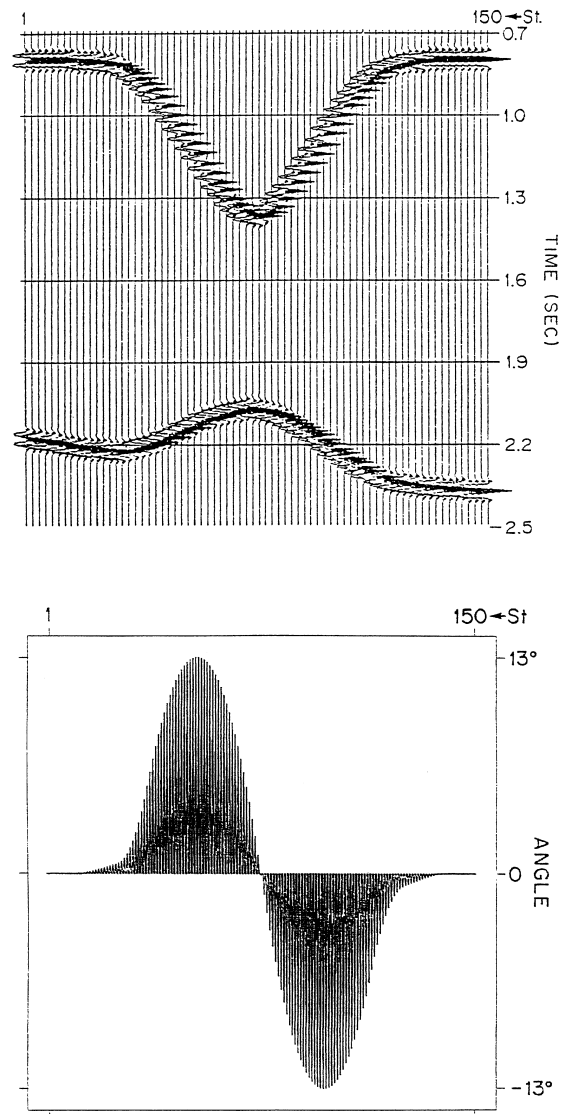


Fig. 5. Calculated time section and kinematical attributes of the first reflector. (a) Zero-offset time section. (b) Angle curve. (c) Radius curve.

corresponds to the point of conjugation of the left plane segment and the adjacent convex arc of the first reflector (Fig. 4). This conjugation looks, on both the model and the stacked field time section, smooth but, in reality, there is a very small area similar to the point of singularity for the first derivative. In this area, the normal to the reflector changes very quickly and is mapped in the HI image as the characteristic point.

The next characteristic point is the curve maximum. This is the image of the left inflection point in which the left convex arc conjugates with the left concave arc. In this case, as in the previous, the inflection point could not be seen in the model or the time section. The third point, in which the angle rapidly changes the sign, is the image of the trough of the syncline. The next two characteristic points on the angle curve are the images of the right inflection and conjugation points.

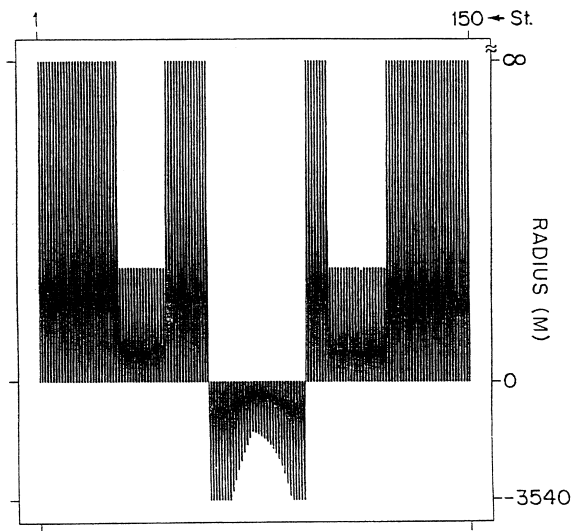


Fig. 5 (continued).

A similar scenario may be observed on the radius curve (Figs. 5c and 6c). The plane segment is imaged by the very large (theoretically infinite) radii, which change rapidly and jump to lower values. This jump corresponds to the first point of conjugation of the plane and curve segments. At the second critical point, the radius curve jumps from low to high values. This point corresponds to the inflection point on the angle curve or the region of rapid change of the sign of the second derivative of the reflecting surface. This critical point was not noticed on the time section. At the third characteristic point, radius jumps from positive to negative values. This point corresponds to the inflection point of the reflector. The fourth characteristic point, the deepest point of the valley in the middle of the radius curve, is the image of the syncline trough. The last three critical points are images of the symmetrical characteristic points of the reflector.

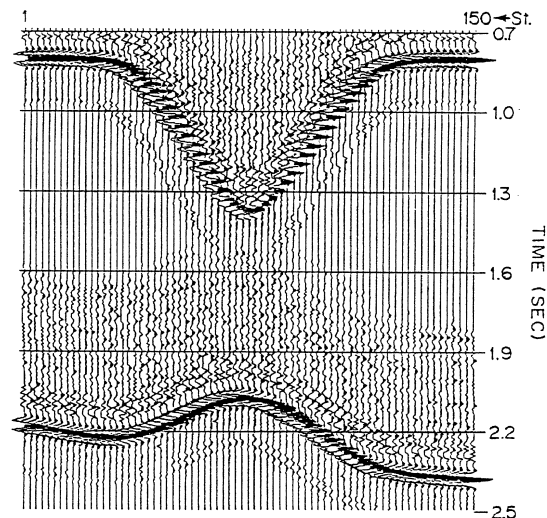


Fig. 6. Time section and kinematic attributes of the first reflector obtained from CEE processing. (a) CEE stacked section. (b) Angle curve. (c) Radius curve.

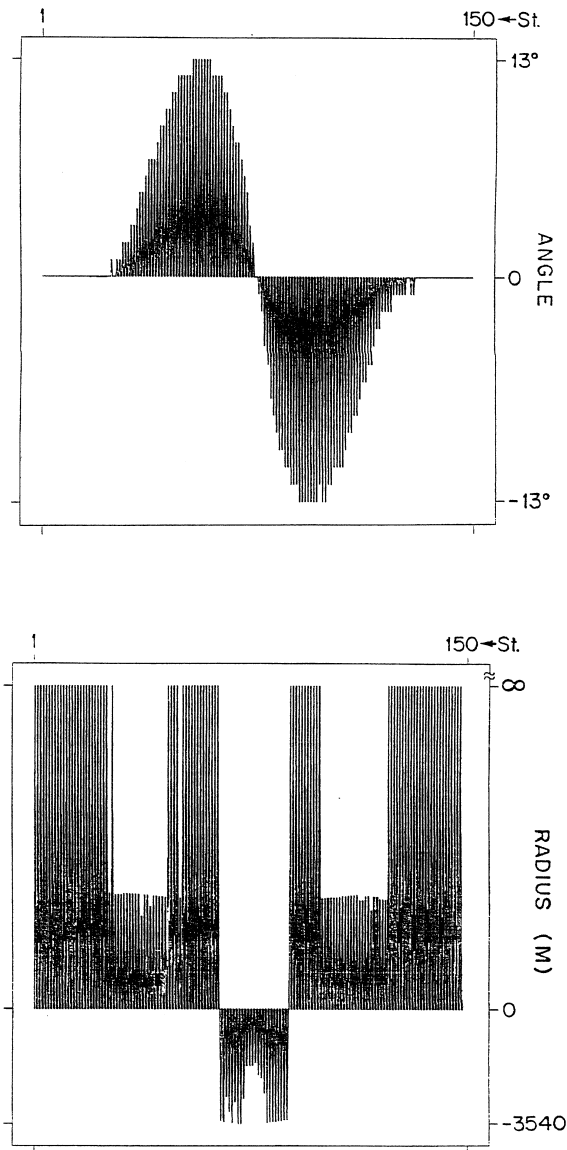


Fig. 6 (continued).

Fig. 7 shows the calculated angle and radius curves for the second reflector. The critical points are also visible on these curves, although the reflector is a slightly inclined plane surface which has no singular point. These points have been “acquired” as a result of passing through the first reflector. This is clearly seen on the angle curve (Figs. 7a and 8a): except for small shifts in their position, the five critical points of the angle curve for the second reflector correspond to the five critical points for the first reflector. The asymmetry of the second curve is caused by the inclination of the second reflector. The radius curve for the second reflector (Figs. 7b and 8b) is more complicated than the angle curve (Figs. 7a and 8a); the characteristic points appear on the radius curve as isolated peaks. However, all seven critical points of this second radius curve can be observed, as on those on the first

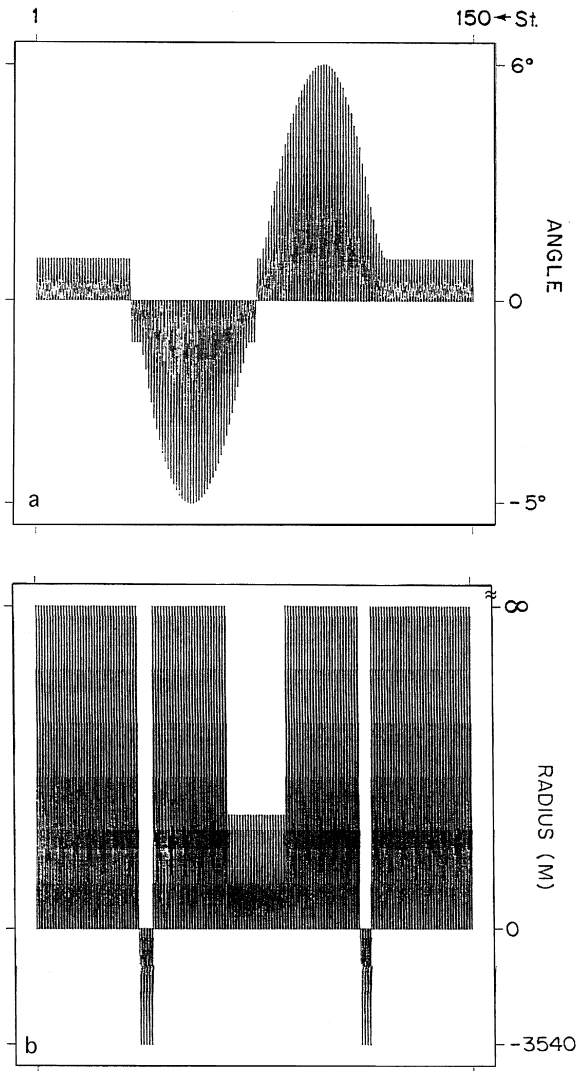


Fig. 7. Calculated time section and kinematical attributes of the second reflector. (a) Angle curve. (b) Radius curve.

radius curve (Figs. 5c and 6c). The coordinates of the corresponding critical points, which should be the same on both the radius and angle curves, are reasonably close to each other (Fig. 7a and b).

The parameter curves for this simple model have been discussed in considerable detail since they illustrate one basic properties of HI clearly, i.e., the conservation of critical points. In topology, it is proved that topological mapping conserves all the critical points of a mapped object. This means that each critical point of the object is mapped into a critical point of its image (homeomorphism). Note that the *type* of the critical point is not necessarily preserved.

Under the assumption that mapping transformation and its first two derivatives are continuous, then each critical point of the HI image corresponds to a critical point of the reflector. However, critical points of the transformation are also mapped into critical points of image. In our HI case, the transformation is accomplished by a reflected wave propagating near the seismic (reference) line. Any critical point a ray of this wave encounters between a source and a receiver is mapped into the HI

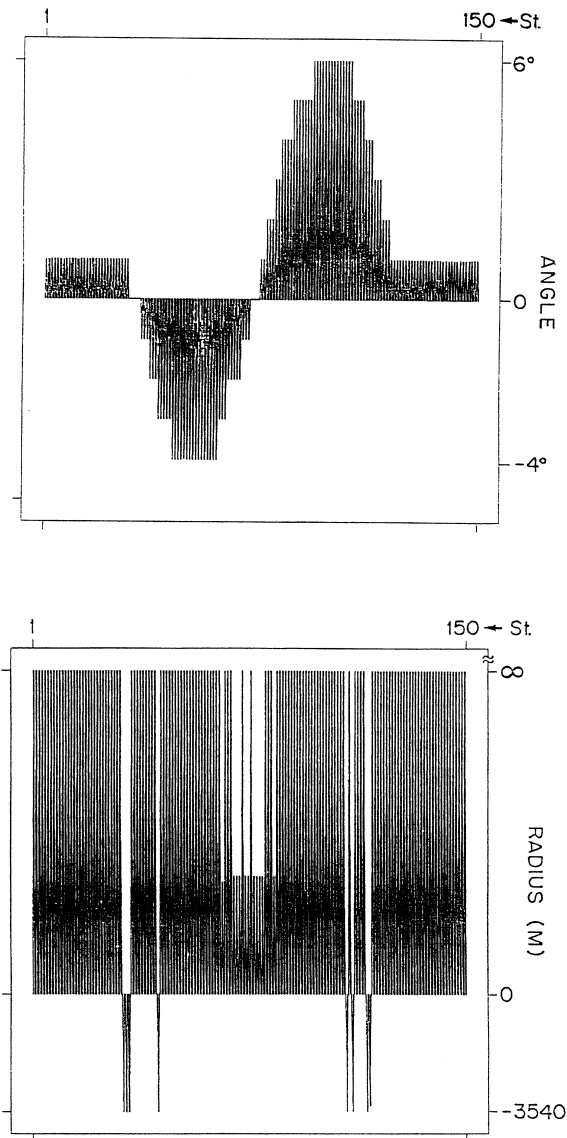


Fig. 8. Time section and kinematical attributes of the second reflector obtained from CEE processing. (a) Angle curve. (b) Radius curve.

image of the reflector. The CEE mapping of the model in Fig. 4 has critical points of both types, thus, not all critical points found on parameter curves of a reflected wave may be attributed to the reflector on which this wave is formed. A combined analysis of the critical points found for the reflector and intermediate interfaces should be carried out in order to identify the critical points belonging to the reflector.

The pattern of critical points of a structure or, more general, a phenomenon — is called its “portrait”. In some branches of modern mathematics — e.g., chaos and the theory of non-linear systems — the portrait is regarded as the most important characteristic of the phenomenon. The portrait of complex systems is used not only in theoretical studies, but also in practical applications.

This concept should hold in a similar way in geology, reservoir engineering, mining, mineral, environmental and other branches of applied geophysics. The disposition of peaks of synclines or anticlines, angle points of interfaces, faults or other structural elements, wedges, closure (inflection) lines, etc., is major target of modern exploration. The HI technique permits us to obtain topologically equivalent portraits of the subsurface by processing seismic data, without making any assumptions regarding structural or physical properties. HI thus is the most reliable way to find the critical points in a medium, trace them and construct their isolines in image space.

It is also worthwhile to consider the following feature of the HI technique. The anglegrams and radiusgrams represent the behavior of the first and second derivatives of reflecting interfaces. Angles and radii are determined not by differentiation of recorded data, but as the optimal parameters by the correlation (summation) procedure. This procedure is similar to integration and is considerably more

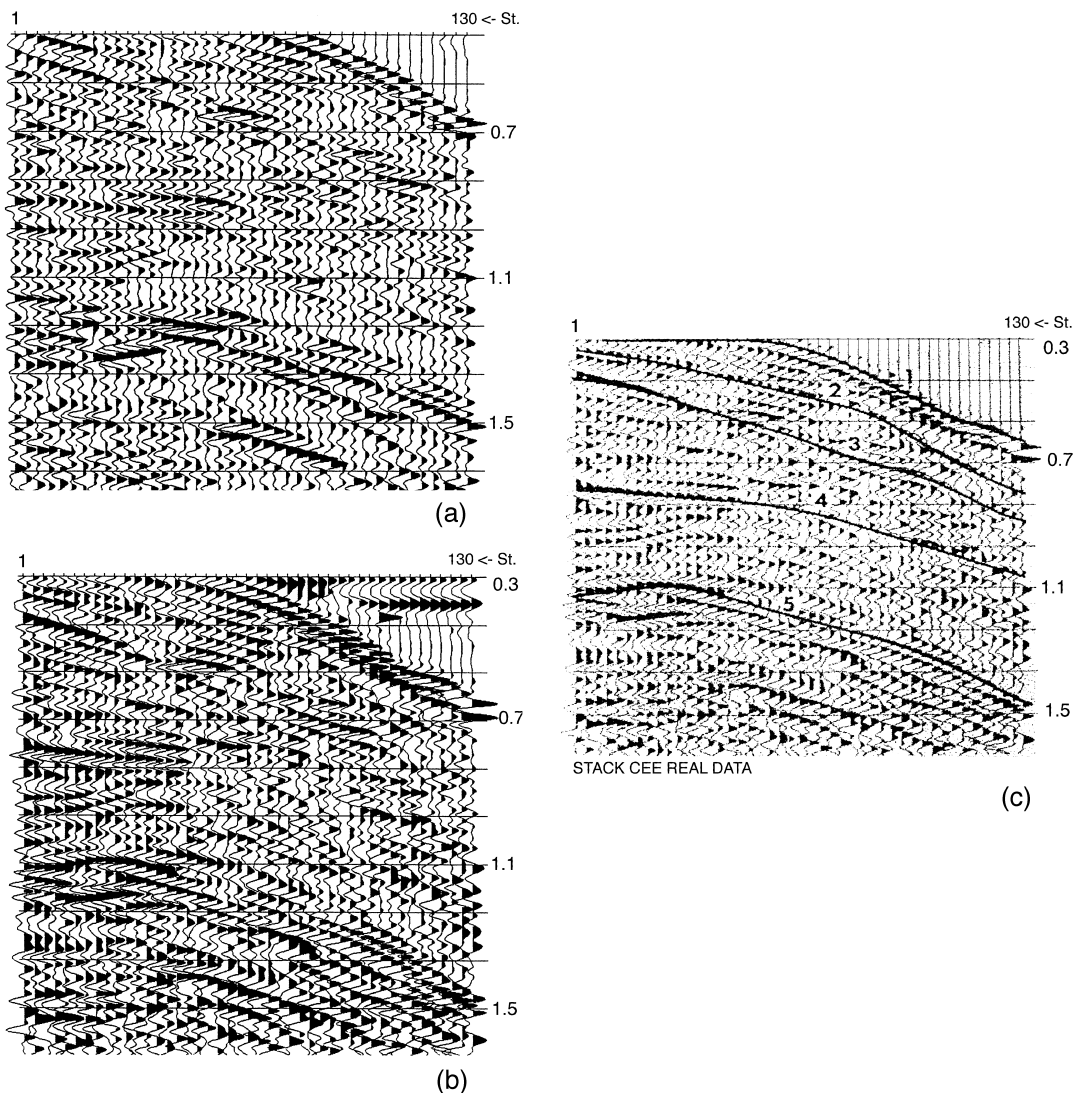


Fig. 9. Time sections of marine data. (a) CMP stacked section. (b) CEE stacked section. (c) CEE stacked section with five correlated waves.

reliable than differentiation. Spatial differentiation of recorded data, or any quantities obtained from it, are not applied at any stage of the HI technique. The isolation of critical is also an important step in solving kinematic inverse problems. This is discussed further down.

Here is the point to discuss a step in HI processing that has been postponed: the decomposition procedure. The HI correlation and stacking procedure results in four (or five) types of time section. Each of these is a continuous 2D function of the position of and time on a central trace. In order to use these sections in the later processing stages, they must be decomposed into parts corresponding to distinct body waves.

This decomposition is achieved as follows: An interpreter interactively traces events on the stacked time section. The program then finds the maximum value of the semblance and corresponding values of time, angle and radius in a fixed window around each picked event. In this way, the arrival time  $t^m(x)$ , angle  $\beta^m(x)$  and radii  $r_{\text{cee}}^m(x)$  and  $r_{\text{cre}}^m(x)$  curves are found, where the superscript  $m$  ( $m = 1, 2, \dots, M$ ) indicates the selected body wave. The collection of the resulting parameter curves is subject analyzed for critical points analysis and serves as input for the subsequent processing steps. As an example, this procedure is applied to a marine data set (Figs. 9–11). The stacked CMP section (Fig. 9a) appears rather complicated. It is not possible to trace any wave with sufficient confidence. The stacked CEE section (Fig. 9b) obtained from near offsets traces differs significantly from the CMP section. Correlation may be attained with more certainty and a new phase lineup appears (Fig. 9c). While the improvement observed on the stacked CEE is essential, it is not drastic. This situation is observed often.

The decomposition procedure was applied to the CEE sections. An interpreter traced five wave lineups shown on Fig. 9c. The decomposition program found the five corresponding collections of parameters curves:  $t^m(x)$ ,  $\beta^m(x)$  and  $r_{\text{cee}}^m(x)$  ( $m = 1, \dots, 5$ ).

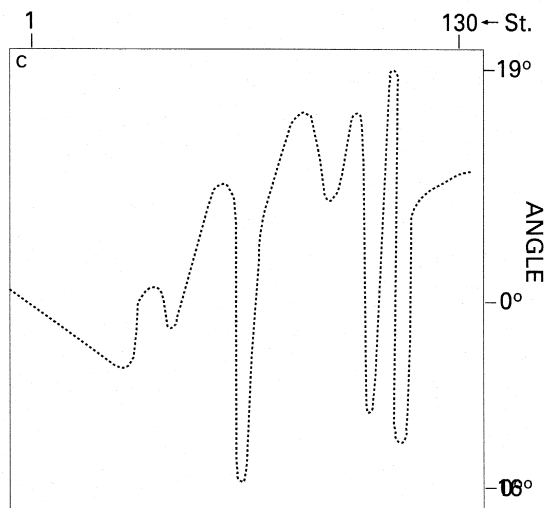
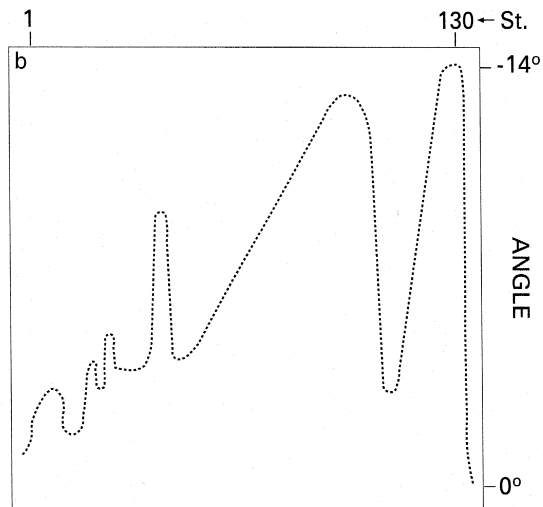
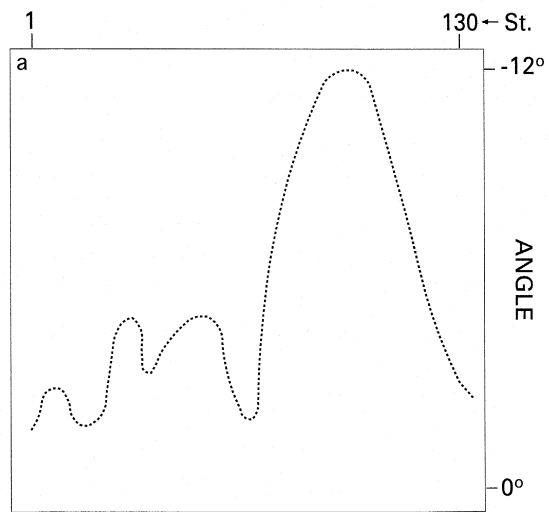
Figs. 10 and 11 show part of the results obtained (sequences of the angle and radius curves subject to their arrival times). In Figs. 10 and 11, some regions similar to neighborhoods of critical points observed for the simple model may be noted (Figs. 6–8). It is possible, to try to determine a corresponding type of interface singularity using the similarity between observed areas and those on the modeling curves. However, at the present stage of HI processing, a reliable basis for determining type of critical regions has not yet been constructed.

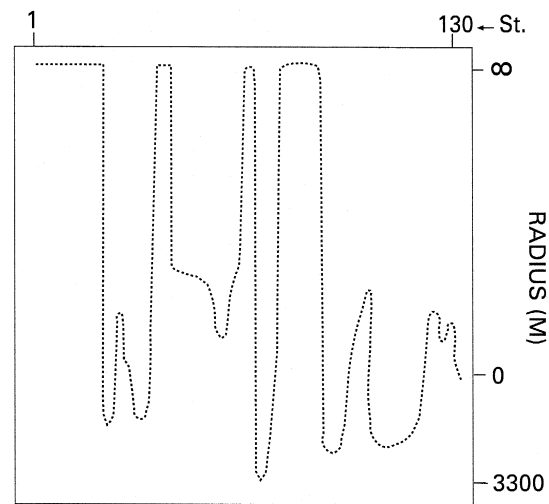
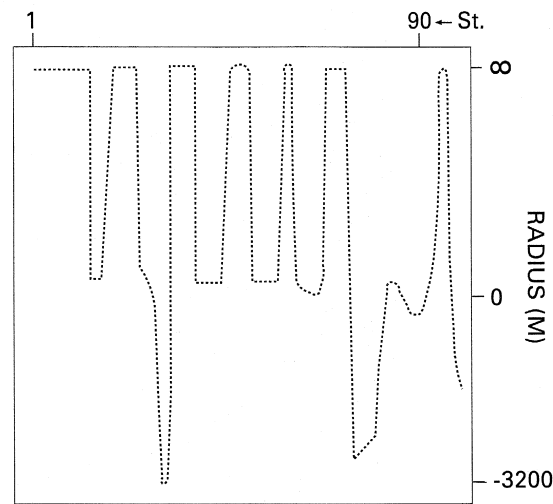
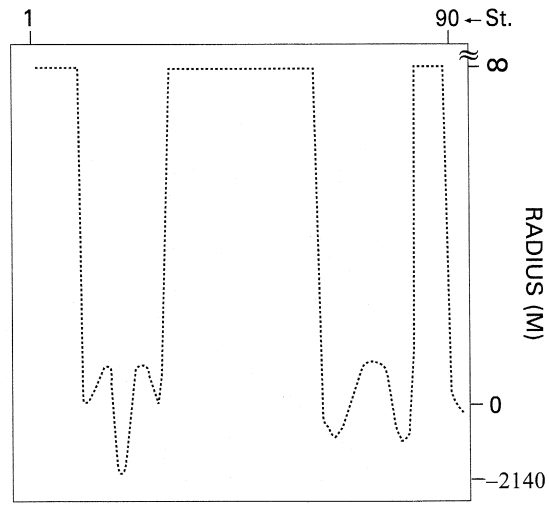
From another point of view, it is feasible and fairly accurate, to pick the vicinities of critical points moving from shallow to deeper interfaces. For example, on the angle curve (Fig. 10a) for the first detected wave, five to six critical regions may be distinguished. On the corresponding radius curve (Fig. 11a), six to seven critical points could be picked out. The next two curves (Figs. 10b and 11b) pertaining to the second reflector appear to be more complicated, but there are some regions that could be critical. Here, two to three new critical points appear. The following Figs. 10c and 11c correspond to the third interface. The angle and radius curves are stronger than for the second interface, but still the critical areas may be isolated.

The discussion here is merely a qualitative examination of the collection of parameter curves obtained in a complex situation by studying the upper part of sediments with rapidly changing structures. In this case, the interfaces have a complicated topography with a dense distribution of critical points. Even in such situation, it seems that critical point analysis could be carried out.

---

Fig. 10. CEE angle curves obtained from the decomposition procedure. (a) Angle curve for the first reflector. (b) Angle curve for the second reflector. (c) Angle curve for the third reflector.





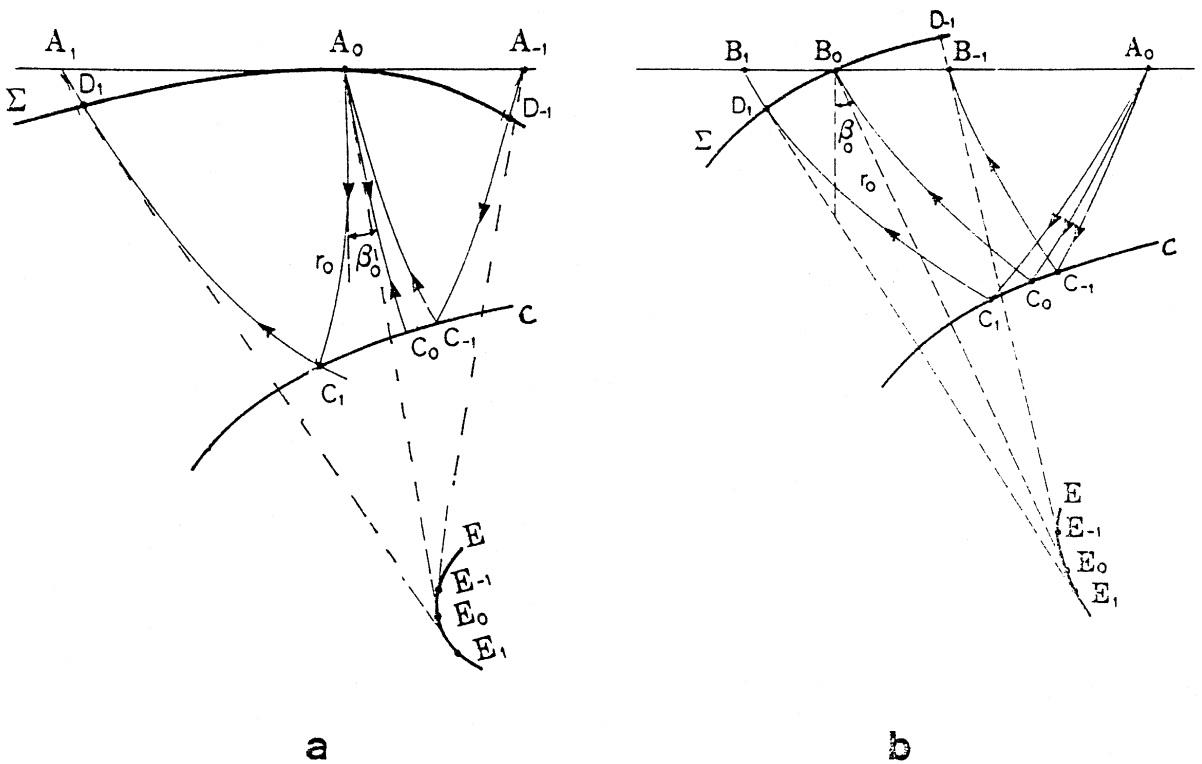


Fig. 12. Ray schemes of CSP method. (a) Ray scheme for the zero-offset section. (b) Ray scheme for the non-zero central trace.

Another example of parameter curves with critical points detected by HI processing of marine seismic data is reported in Gelchinsky et al. (1993).

## 5. Results of different HI methods

### 5.1. The CSP HI method

Before discussing the results, the CSP (or common receiver point [CResP]) and combined HI methods are considered briefly. The ray scheme of the CSP method is shown in Fig. 12. The wave front on which this method is based is the real reflected front  $\Sigma$  in the seismic acquisition (Keydar et al., 1996). The time correction is determined by the relation

$$\Delta\tau_k = \tau(A_0 C_k A_k) - \tau(A_0 C_0 A_0) = \left( \left[ r_{\text{csp}}^2 + 2 \sin \beta_0 r_{\text{csp}} \Delta x_k + \Delta x_k^2 \right]^{1/2} - r_{\text{csp}} \right) / v_0 \quad (17)$$

Fig. 11. CEE radius curves obtained from the decomposition procedure. (a) Radius curve for the first reflector. (b) Radius curve for the second reflector. (c) Radius curve for the third reflector.

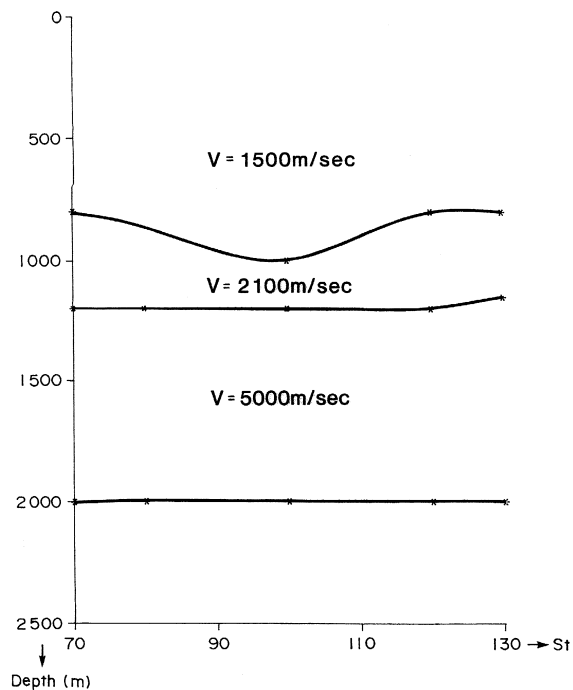


Fig. 13. Three-layer model.

where

$$\Delta x_k = A_k A_0 = x_k - x_0 \quad (k = 0, 1, \dots, n). \quad (18)$$

The time correction formula is written in the spherical approximation of the front  $\Sigma$ , although in Fig. 12 this front is shown as non-spherical. The formula for a non-spherical front has as additional parameter, i.e., the radius of the caustic  $E$  (Gelchinsky and Keydar, 1993).

The method has been tested with the synthetic data based on the three-layered model of Fig. 13. The results of processing with the CSP method are shown in Figs. 14–22. The CSP travel time curves are far from hyperbolic in shape (Fig. 14), but this is no serious obstacle to the CSP correlation and stack (Fig. 17). The calculated zero-offset time section (Fig. 15) and CSP time sections are close, while the CMP images of the second and third (partial) reflectors are noticeably distorted (Fig. 16).

The color anglegram and radiusgram are presented in Fig. 18. Their backgrounds are different because the in the radiusgram only those radii corresponding to semblance values which are greater than threshold of 0.5 are shown. Use of a threshold suppresses noise and improves the general appearance, but degrades the image of useful waves in areas of low semblance, e.g., in the vicinity of critical points. This effect is seen on the radiusgram in the “holes” in the images of the two lower reflectors below the triplication of the first reflector. The colored anglegram and radiusgram can be used to define the general behavior of angles and radii of associated fronts and for a rough location of critical points. These are likely to exist in regions of strong color contrast, or near points sharply distinguished from the surrounding background.

In Fig. 19, the of homeomorphic images of the three reflectors described previously in the discussion of the CRE method are shown. A rib of each “fence” is the HI of the reflector. The image of the triplication of the travel time curve of the first reflector appears as an isolated island.

The decomposition procedure resulted in the parameter curves shown in Figs. 20 and 21. The triplication of the travel time curves and the corresponding part of the angle curve with two modes are

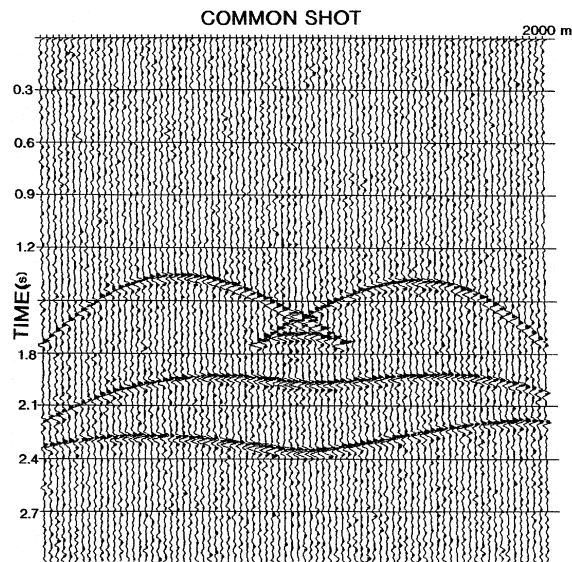


Fig. 14. A typical CSP gather.

clearly seen in Fig. 20. The two radius curves (Fig. 21a and b) were determined using the CSP method and CEE technique, respectively. They are rather complicated, but the characteristic points can easily be found. Some of these *critical points of the radius curves* may be connected with *critical points of reflectors*.

The discussion of the CSP method is concluded with an example in which the stacked time sections obtained by CMP and CSP processing, respectively, of real data (Fig. 22a and b) can be compared. Even cursory inspection shows that the quality of the CSP section is considerably higher than that of the CMP section. In this simple case, the difference was probably caused by different number of

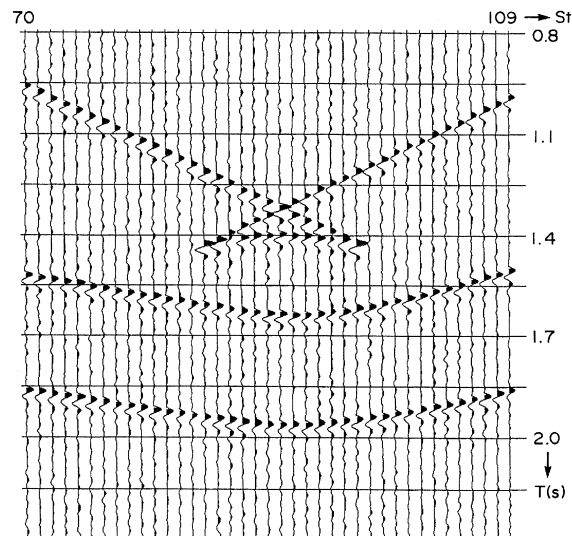


Fig. 15. Zero-offset time section.

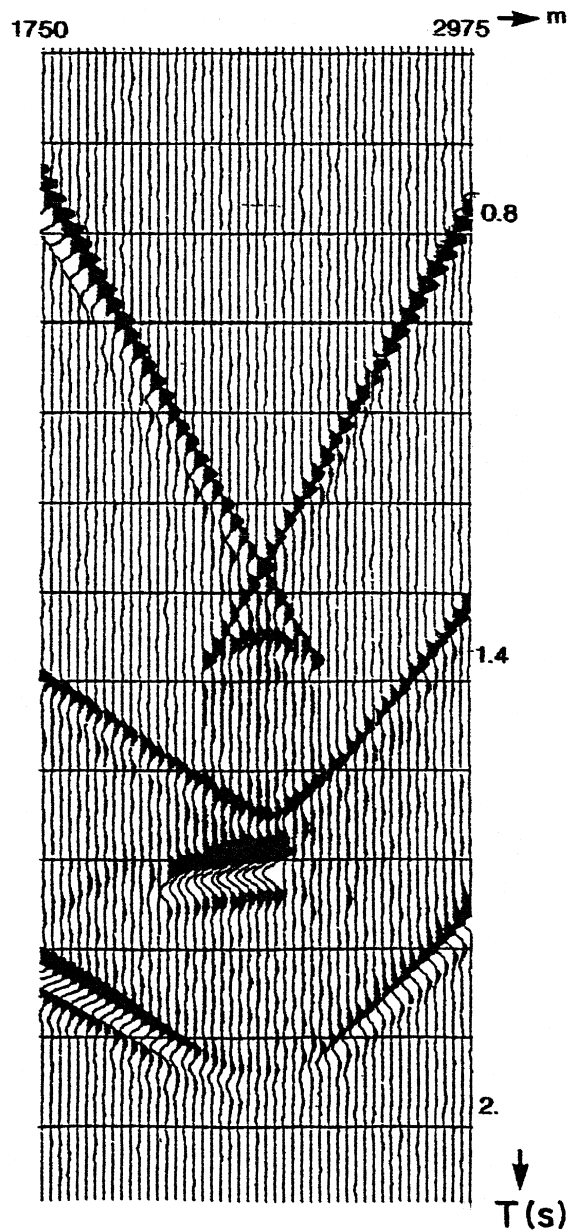


Fig. 16. CMP stacked section.

traces stacked in each CSP and CMP gather, respectively. Experience shows that the difference between the conventional and HI stacked sections increases with the complexity of the structure. In simple cases, both sections are rather similar.

### 5.2. The combined HI method

The HI method described above are each based on a specific distribution of source–receiver pairs and a special time correction formula. Each of them is applied individually, thus, four types of time

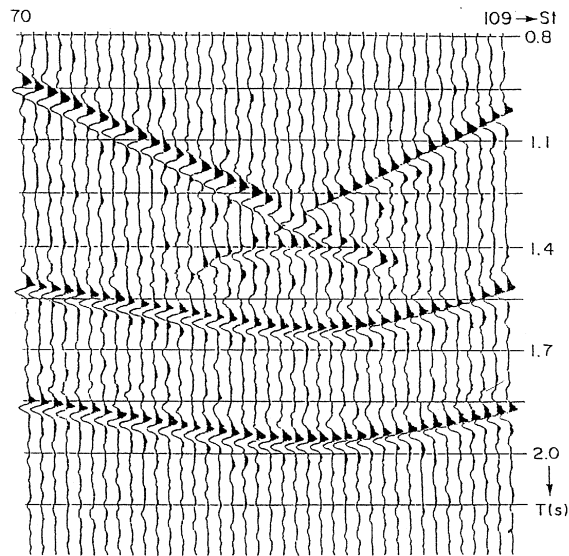


Fig. 17. CSP stacked section.

section are produced. All should be decomposed into parts corresponding to separate types body waves. During the interpretation process, the complicated question of identifying the same event on the sections obtained using the different HI methods arises. The solution to this problem could be considerably simplified if the different types of correlation and stacking were combined into one operation (Keydar et al., 1993). There are three major schemes for combined operation: *parallel*, *sequential* and *mixed stacking*. Only the mixed scheme was tested and, therefore, our discussion centers on this.

The combined scheme consists of two stages: first, parallel stacking of data corresponding to central points according to one or more different HI (CRE, CSP, etc.). These stacks produce the four types of HI section, among them, the stacked wavefield section which is the first approximation of the zero-offset section. The second stage is the CEE stack in which the input is the zero-offset section obtained in the first stage. The output of the second stage is the next approximation of the zero-offset time section, as well as the semblancegram, the anglegram and the CEE radiusgram.

The CSP (or CEE or CRE) gather is input in each parallel stack of the first stage. For example, performing the CSP stack in each source position, one could use all recorded traces. The output of this stack is plurality of zero-offset traces obtained for each shot. By collecting all the traces in the vicinity of each fixed center point, the second stage (the CEE stack) can be accomplished. The disadvantage is that each parallel stack of the first stage is performed independently using traces belonging to only one CSP gather. This means that the reliability of such correlation and the stack method is much lower than that obtained when using all traces relating to one central point simultaneously. This disadvantage is common to all the methods discussed above.

Figs. 23a–c and 24a–c show output of the first and second stage of the combined HI method, respectively, for land data. Obviously, the quality of the stacked sections of the second stage is much higher than that of the corresponding section after the first stage (Figs. 23a and 24a). It is interesting to note that the frequency content of the combined time section is much richer than that of the

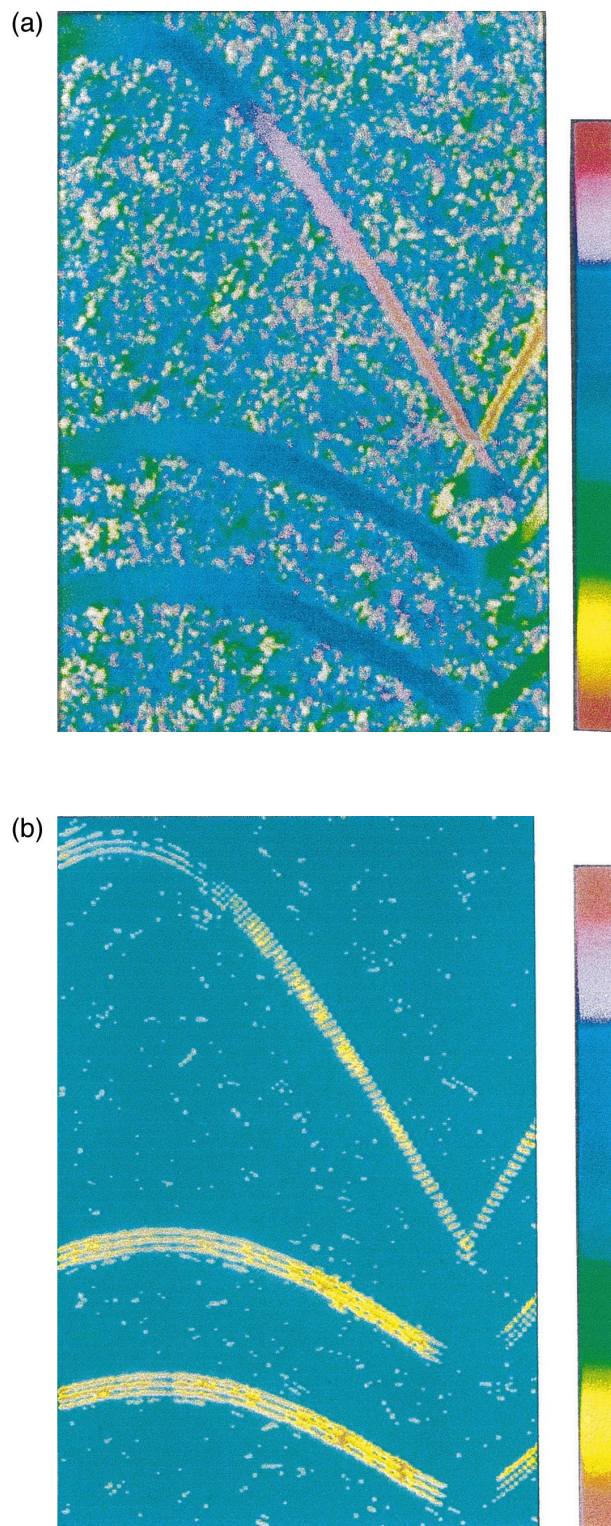


Fig. 18. CSP anglegram and radiusgram. The values of the angles and radii represented by colors. (a) Anglegram (without semblance threshold). (b) Radiusgram (with semblance threshold).

## HOMEOMORPHIC IMAGE

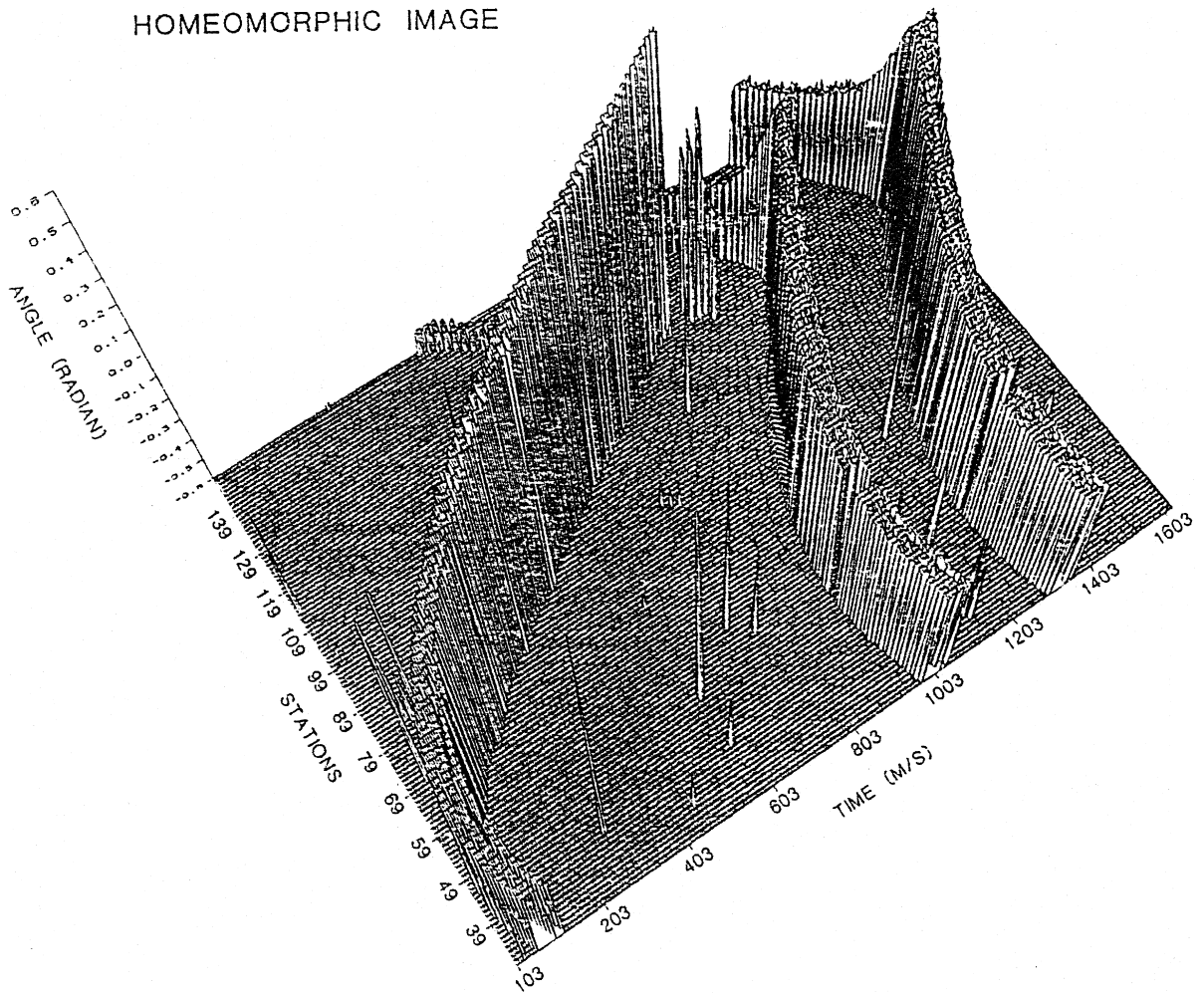


Fig. 19. Homeomorphic image of three reflectors as function of angle, time and  $x$ -coordinate. A rib of each “fence” is the group homeomorphic image of the corresponding reflector.

recorded traces which are the input for the stack procedure. The same phenomenon can be observed from the different HI. When comparing the CSP and combined anglegrams (Figs. 23b and 24b), it should be borne in mind that they should be similar. Indeed, the main low frequency waves do appear in both figures. However, these waves are clearer and can be traced more accurately in the combined anglegram. Waves with a high frequency content which can be traced with relative ease on the stacked combined time section (Fig. 24a), can be picked out and traced only with difficulty on the anglegram (Fig. 24b). This phenomenon could be connected with the observation that in areas *without* strong interference the anglegram resembles an envelope. This is also noted on anglegrams obtained using different HI methods without strong interference.

Comparing the corresponding time sections, one should keep in mind that each wavefield section (anglegram) after the first and second steps represents the zero-offset time section (the same distribution of radii of the wave front). The distribution of radii of the CSP and CEE

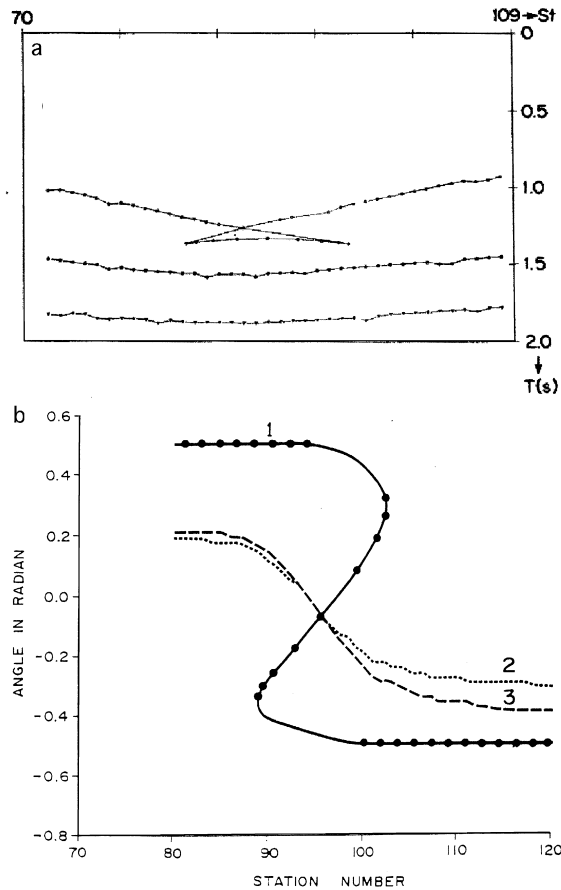


Fig. 20. (a) CSP travel time curves obtained by the decomposition procedure. (b) CSP angle curves obtained by the decomposition procedure. There is a good correspondence between the critical points of the travel time and the angle (turning points) curves.

wave fronts should be different, as it seen on the Figs. 23c and 24c. The quality and the resolution of the radiusgram after the second step is much better than after the first step. However, the large difference in frequency content of the radiusgrams after the first and second step is surprising.

The CSP and CEE radiusgrams (Figs. 23c and 24c) differ considerably. The apparent frequency on the CEE radiusgram is about 70–90 Hz, but wave phases of such high frequency can be traced without any difficulty. The apparent frequency on the CSP radiusgram is much lower and the wave correlation properties much poorer than on the CEE radiusgram, although the main wave package could be identified on the CSP and CEE time sections (Figs. 23a and 24a).

The combined HI method significantly improves the picking of wave packages and their correlation. Though the interest has shifted to the multifocusing method there are valid reasons to include the combined method in the general scheme of HI data processing.

### 5.3. Comparison of different HI methods

The different HI methods have been tested with for the relatively complicated model in Fig. 25. Some illustrations of the processing are also shown (Figs. 26–30). These have been selected from

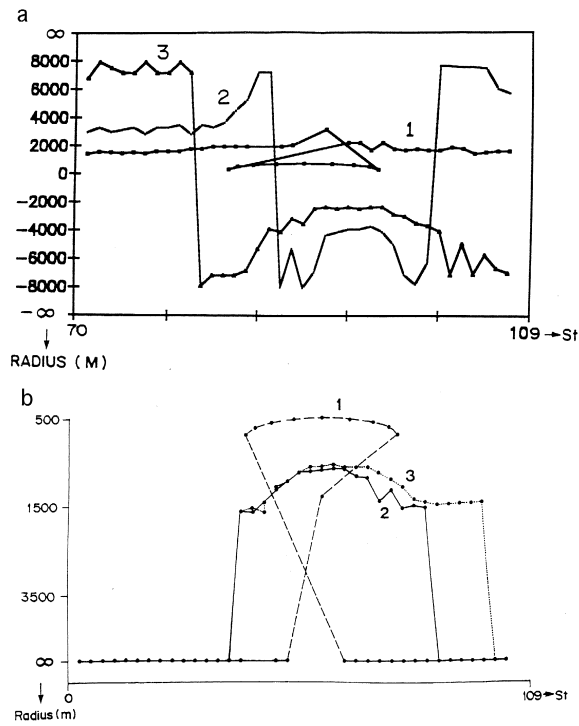


Fig. 21. (a) CSP radius curves obtained by the decomposition procedure. (b) CEE radius curves obtained by the decomposition procedure. There is a good agreement between the CSP and CEE critical points, although normally the CEE radius curve has more critical points than on CSP curve.

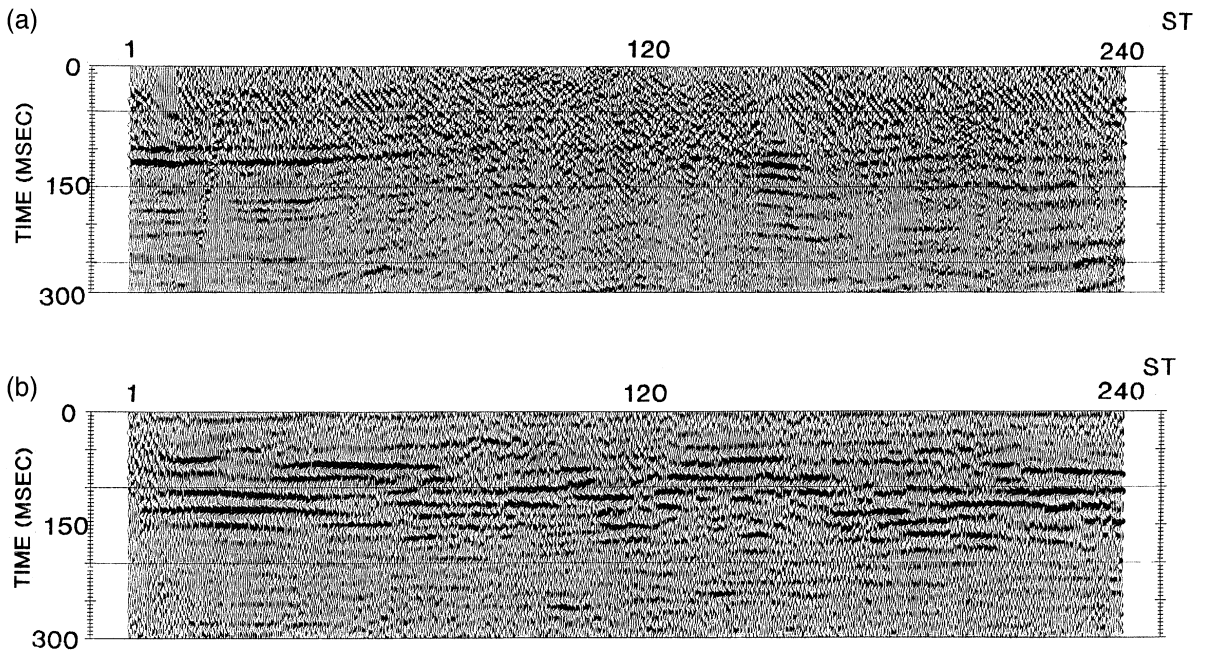
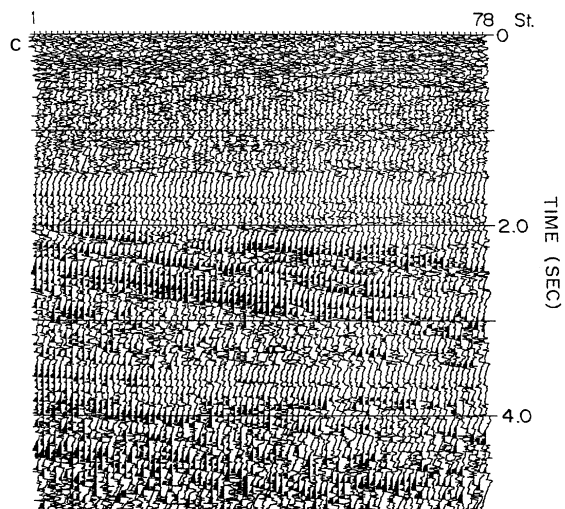
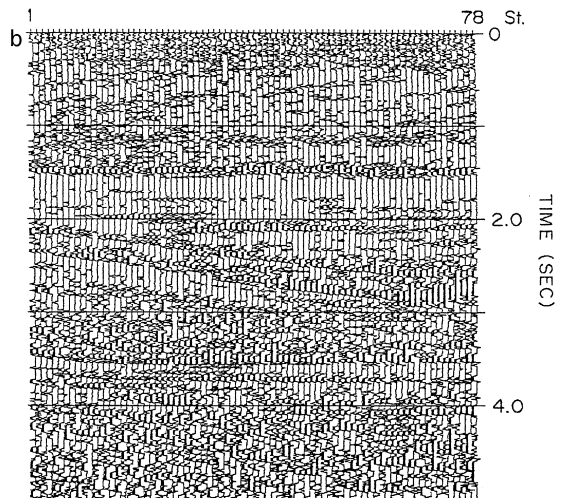
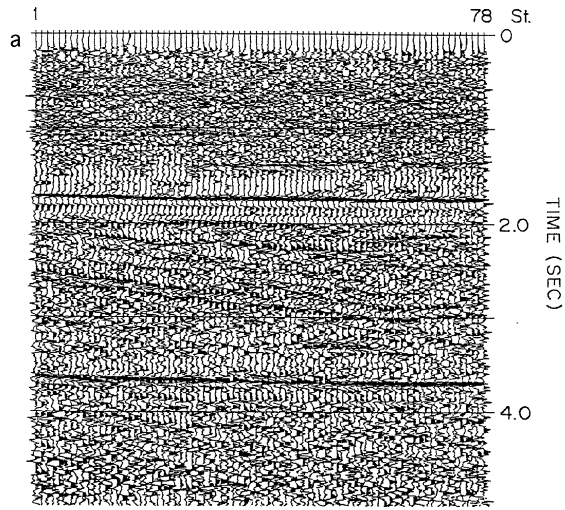


Fig. 22. Stacked time section of real land data. (a) CMP stacked section. (b) CSP stacked section.



material obtained by CMP, CSP, CEE, combined, and multifocusing some of the material was presented by Keydar et al. (1993), and in a thesis by Berkovitch (1995). In Figs. 26 and 27, the calculated zero-offset and stacked time sections obtained with different data processing methods are shown. The main properties of the zero-offset time section are clearly mapped in all time sections presented; however, the CMP section has several disturbances marked on Fig. 26b. In the CSP and combined time sections, no disturbances are visible (Fig. 27), and the combined section is very close to the zero-offset section. The combined semblancegram is shown in Fig. 28. Fig. 29 shows the combined anglegrams. It can be seen that the angles of entry of all three waves change rapidly in many regions, not only those related to loops. The CEE radiusgram obtained through combined processing are shown in Fig. 30.

The comparative analysis of the results of the CMP, CSP, and combined data processing leads to the following conclusion: If a structure is not very complicated, (or rather, if there is no strong interference of waves with similar kinematic parameters) the CMP and HI stacked time sections resemble each other, although their description and reliability is different. The reliability level (semblance values) is much higher for all types of stacked HI time section than for the CMP time sections. In some cases, the subsurface could be better traced on the HI semblancegrams than on the stacked HI sections.

The vicinity of critical points is much more clearly distinguished on the HI time sections than on the CMP sections. Combined analysis of different types of HI time sections significantly simplifies the isolation of critical points and tracing horizons. Angle and radius curves could be constructed with relative certainty; however, the accuracy of such constructions is very difficult to estimate. Numerical estimation in modeling shows that the precision of the determination of the angle and radius of smooth parts of the curves is quite high, provided that there is not strong wave interference. The accuracy in the vicinity of critical points lower because the current HI correlation technique is intended for smooth (regular) parts of the wavefield. The special HI method for detecting and location angle points is one exception, but the “regular” correlation of HI procedures detects critical points quite well.

The best way to evaluate the accuracy of the parameter curves is by solving the kinematic inverse problem. If a “true” seismic model can be constructed with sufficient accuracy, using the angles of entry and the CRE and CEE radii, then the precision the HI correlation technique is satisfactory.

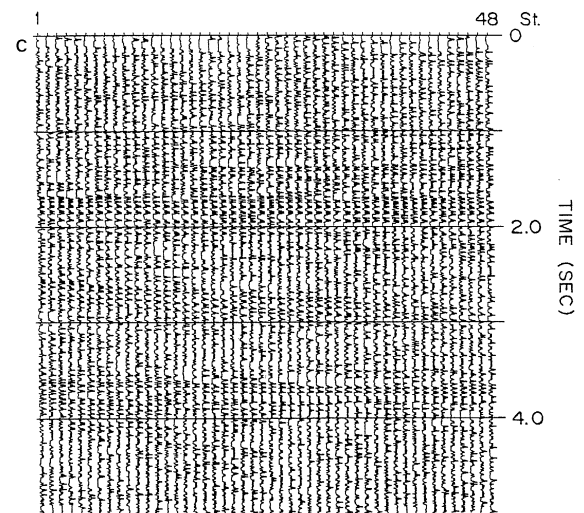
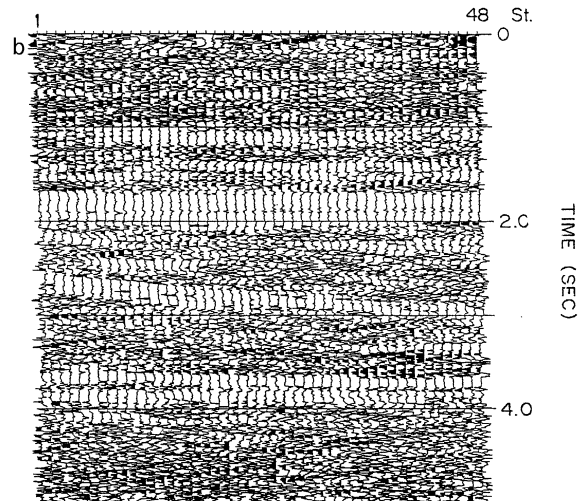
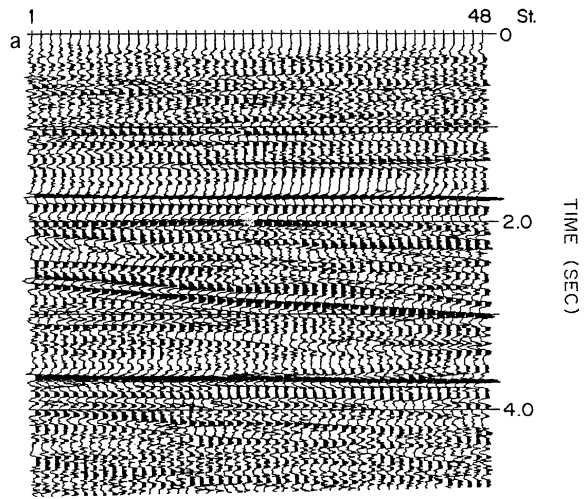
#### 5.4. Application of the CRE method

The CRE method was not only the first HI technique created, but also the first tested. Many interesting results were obtained using this technique (Gelchinsky, 1988, 1989; Koren and Gelchinsky, 1989; Rabbel et al., 1991; Steentoft and Rabbel, 1992; see also reports presented by the Geophysical Institute of the Christian-Albrechts University of Kiel in 1991–1995 for the DEKORP Program and reports by Wainstein et al. for the Israel Ministry of Science).

The CRE method was applied on the Marmousi data (Steentoft and Rabbel, 1994). The Marmousi model contains 160 reflectors, some with steep dips and strong vertical and lateral variations. All data regarding the velocity structure of the model, seismic field calculation and related problems are

---

Fig. 23. Real data. Time sections obtained after the first step of CSP procedure — of the combined HI approach. (a) CSP stacked section. (b) Anglegram. (c) Radiusgram (previous pages).



contained in the Marmousi Experience Proceedings (1990). The Marmousi data is used for testing different seismic imaging and migration methods. In contrast to almost all other tests which use a priori velocity information, CRE processing was applied without this information. The results of the CRE application and comparison with the DMO corrected CMP stacked section are discussed in the paper by Steentoft and Rabbel (1994). Their conclusions are:

- The coherency of the CRE derived image was superior to the CMP stack.
- The CMP and CRE stacked time sections tend to be very similar if the reflectors are continuous.
- The CMP time section appears more smoothed than the stacked CRE section. Hence, in many regions of discontinuity, the CRE semblance values are large and there is reason to believe that these discontinuities are not artificial.
- The diffracted waves are seen more clearly on the CMP section.

The combined stacked sections and angle section are shown in Fig. 31, the combined stacked section and radii section in Fig. 32. The colors are distributed along the reflections in a rather orderly fashion. Many strips of constant color may be noted. This means that in this region the angle of emergence and the CRE radius change gradually. Occasional small areas of rapid color change apparently relict of the regions of critical point. However, the quality of the color images does not allow us to draw any detailed conclusions. Examination of numerical results confirms the previous conclusion: the accuracy of determination of the angles and radii by the CRE method is, in general, satisfactory for quantitative consideration but not satisfactory for solving the kinematic inverse problem. There are — particularly diffracted — waves which have significantly deteriorated.

It is unlikely that the angles of entry and radii obtained with the CEE, CRE, CSP, and similar methods could in their present form be used as initial data in the kinematic inverse problem for complicated structure. However, the use of the angle and radius curves could significantly raise the level of interpretation of processed seismic data.

## 6. Multifocusing HI

The multifocusing HI method from the general problem connected with multifold acquisition of seismic data: a set of  $n$   $m$  traces is recorded in the vicinity each central point, if each CSP gather consists of  $m$  traces and  $n$ -fold coverage is used. In the conventional method and in the HI discussed until now, correlation- and stacking-gathers consist only of  $n$  or  $m$  traces; thus, a significant number of traces connected with the central point is not used in simultaneous seismic data processing. Attempts to create methods with high multiplicity always met with this principal difficulty: each wave field

$$u(A_j^-, A_i^+, t) \quad (i = 0, 1, \dots, m - 1; j = 0, 1, \dots, n - 1) \quad (19)$$

recorded “in situ” during a physical experiment with  $A_j^- = \text{constant}$  corresponds to the solution of a wave propagation problem, i.e., the solution of an equation of motion under initial and boundary conditions. In particular,  $u(A_j^-, A_i^+)$  with  $J$  fixed satisfies the equation of motion. However, a gather of traces  $u(A_j^-, A_i^+)$  with both variable source and receiver points  $A_j^-$  and  $A_i^+$  does not represent a physical experiment and does not satisfy the wave equation with initial and boundary conditions.

Fig. 24. Time sections obtained after the second step, namely, CEE procedure, or the combined HI approach. (a) CEE stacked section. (b) Anglegram. (c) Radiusgram (previous pages).

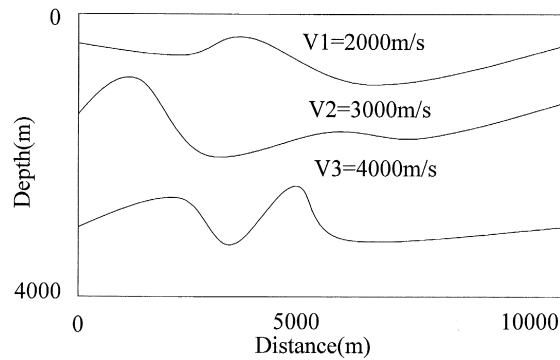


Fig. 25. Three-layer model used for the comparative analysis of the different HI processing methods.

Thus, one cannot use properties of the solution for stacking (or averaging) traces of a gather since, in the first place, it relates to time correction. No solution is known for a total wavefield. However, it is possible to average partial wavefields corresponding to a single type of body wave, provided a time correction formula is found. The major difficulty is of the same nature as for the total field: the eikonal  $\tau(A_j^-, A_i^+) = \tau_{ij}$  depends on the two variables  $x_j^-$  and  $x_i^+$  — the coordinates of two moving points  $A_j^-$  and  $A_i^+$ . In all conventional and HI methods discussed so far, the solution is found as follows: the configuration of source–receiver pairs is selected in such a way that a family of corresponding rays emitted by the sources and/or arriving at the receivers is orthogonal to one real or fictitious associated front. This means that the corresponding arrival times (or time increments) satisfy an eikonal equation with one initial conditions, corresponding to a fictitious experiment. As seen before, it is then easy to find the time correction formula using the geometry of the front.

The first step in the generalization of this approach was made by Gelchinsky and Keydar (1993). They proposed to use configurations of sources and receivers such that two families of rays — one leaving the sources, the other arriving at receivers — form two pencils with an orthogonal front in the vicinity of source and receiver locations, respectively. This type of mapping may be applied in rather general situations, with sources and receivers distributed on arbitrarily smooth curves lying in a vertical plane, and a central ray non-normally reflected (Fig. 33). This type of HI mapping is associated with the two fictitious fronts: one leaving a source line and the other arriving at a receiver line. Thus two images are constructed. Two-image HI mapping is also used in the CCE method (Gelchinsky, 1989; Gelchinsky et al., 1992). This modification enlarges the number of traces used by stacking, though still does not use *all* traces recorded in the vicinity of a fixed point. The generalization which permits the stacking of all rays was proposed by Berkovitch (1995), Berkovitch et al. (1994), and Gelchinsky et al. (2000a; b) and called the multifocusing method. Here, we present the basic concepts and scheme of the HI multifocusing method.

Each event (i.e., each reflected wave) recorded on a trace can be associated with a ray of a corresponding wave. Thus, a set of traces produced by a multifold acquisition system in the vicinity of the fixed central trace can be associated with the fixed central ray and a set of rays belonging to the vicinity of this ray. The proposed multifocusing generalization of HI mapping consists of the association of any pair of traces and  $u(A_j, A_i^+, t)$  ( $i = 0, 1, \dots, m - 1$ ;  $j = 0, 1, \dots, n - 1$ ) with a certain tube  $T_{ij}$  surrounding the central ray (Fig. 34). The two reflected rays  $A_0^- C_0 A_0^+$  and  $A_j^- C_{ij} A_i^+$  are such a pair. The cross-sections of the associated ray tube  $T_{ij}$  at the end points  $A_0^-$  and  $A_0^+$  of the central ray (the front elements) are orthogonal to both selected rays.

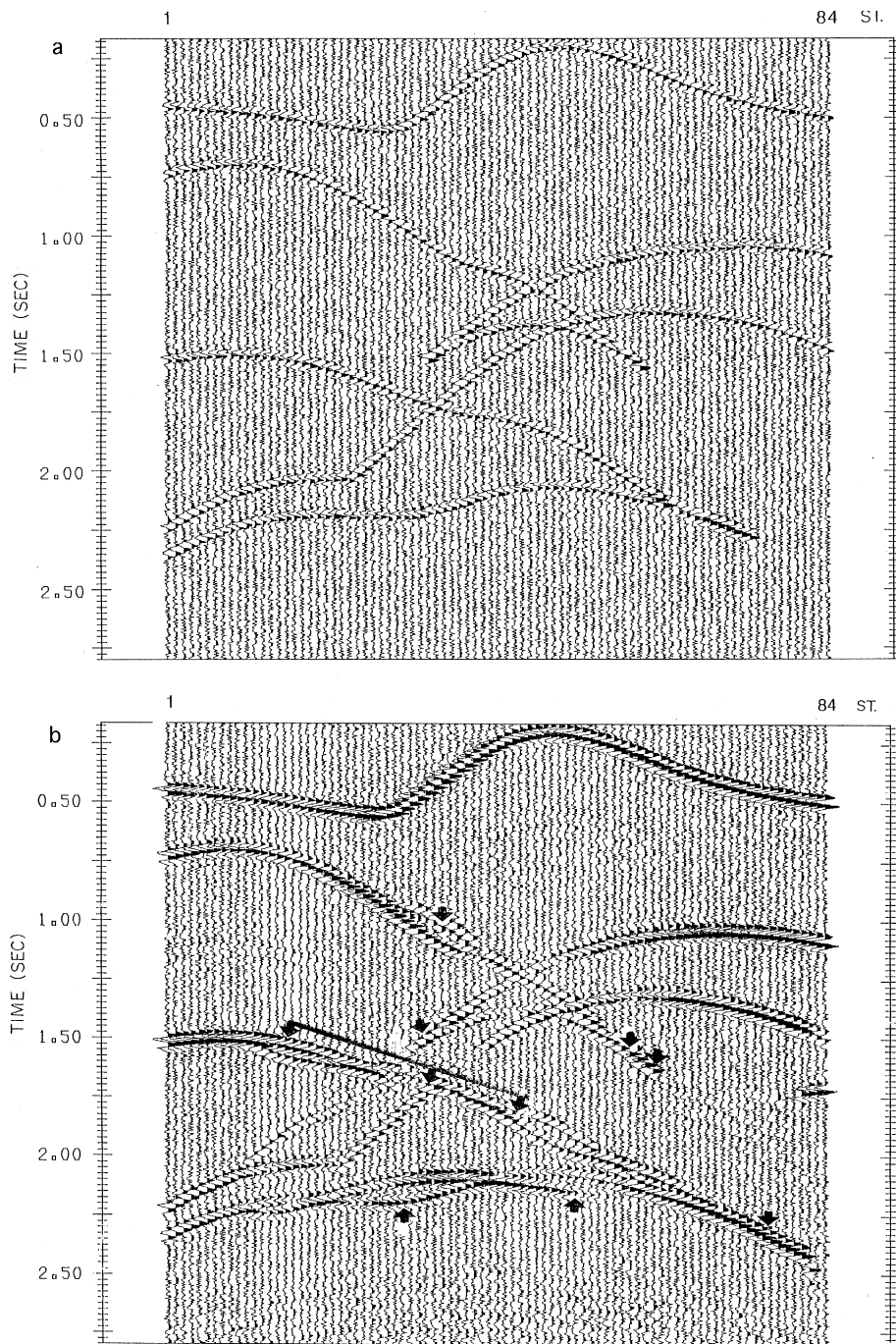


Fig. 26. (a) Calculated zero-offset section for the model in Fig. 25. (b) Calculated CMP stacked section for the model in Fig. 25.

In order to establish this association, the unique correspondence between the source and receiver offsets and the curvatures of the two wavefronts forming the cross-sections of the ray tube  $T_{ij}$  must be

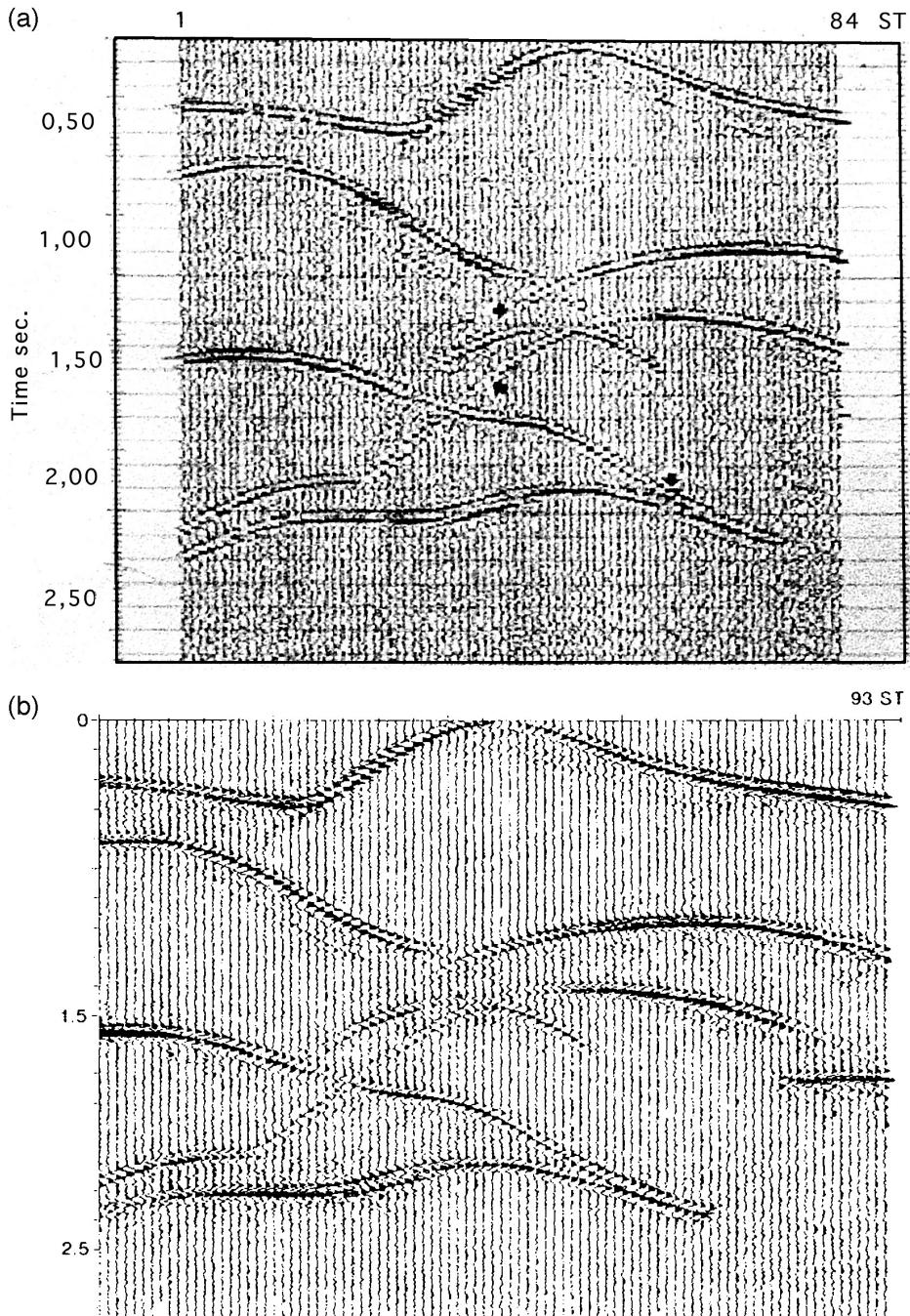


Fig. 27. (a) CSP stacked section for the model in Fig. 25. (b) Combined stacked section for the model in Fig. 25.

found. Those curvatures are called dual curvatures. For this, the geometry of all possible wave fronts at the end points of the central ray is considered. The geometry of the set of fronts is important for seismic processing because the time-correction formula for the trace pair can be expressed in terms of

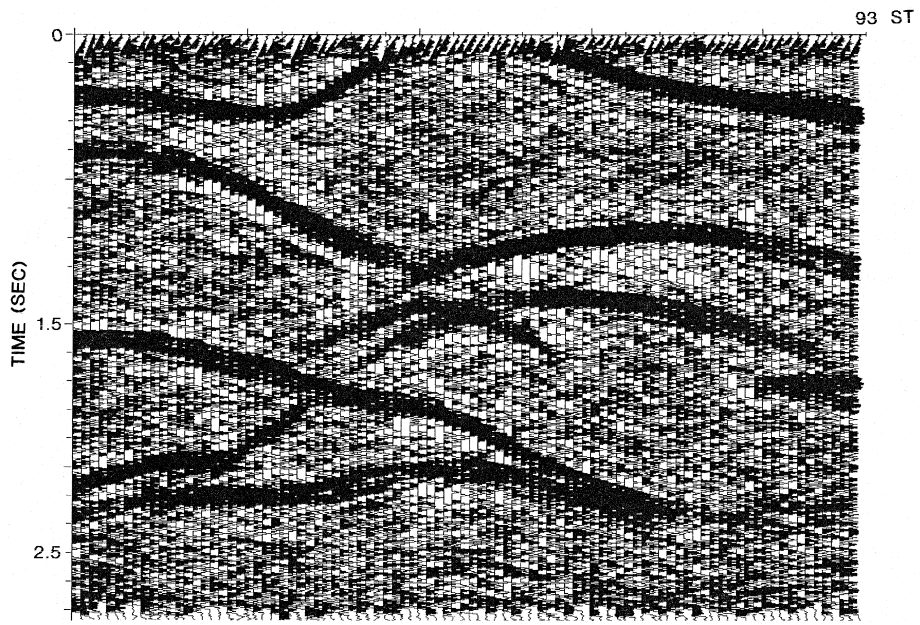


Fig. 28. Combined HI semblancegram.

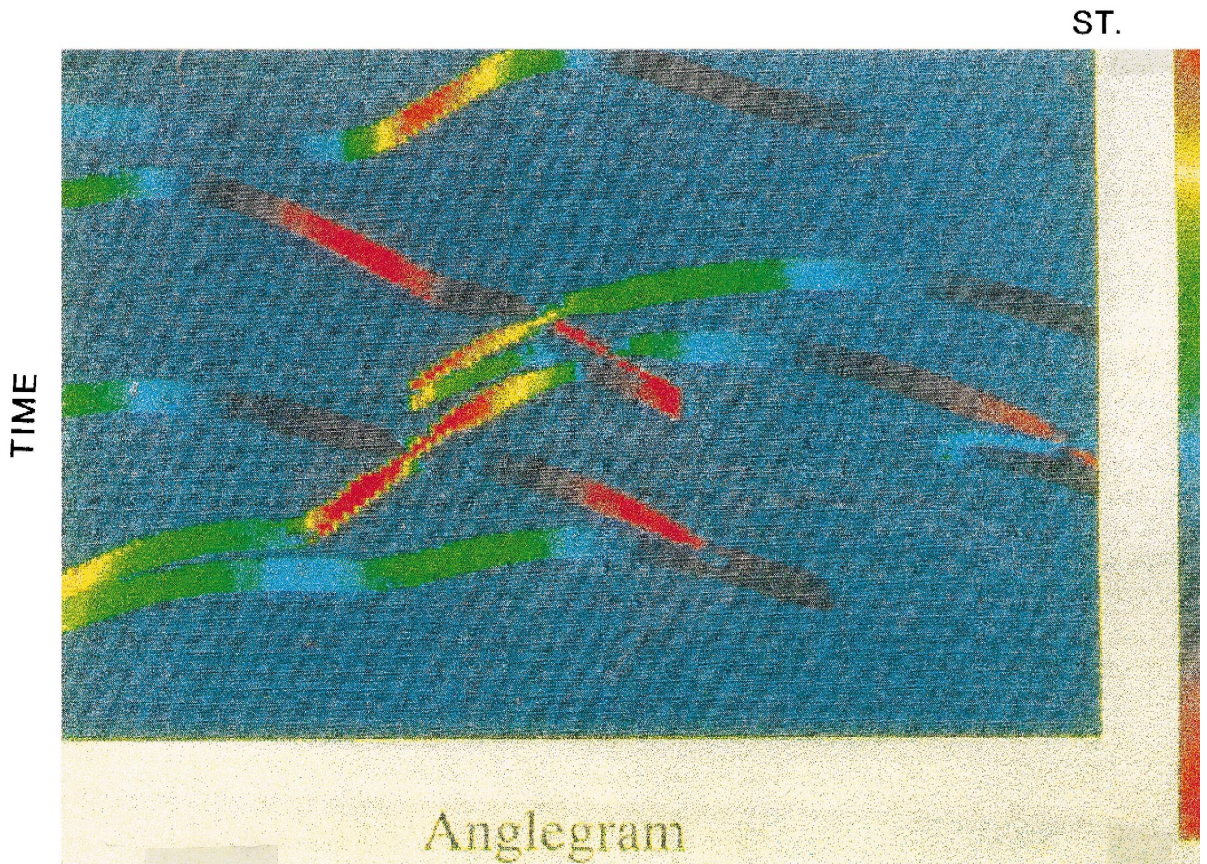


Fig. 29. CSP anglegram.

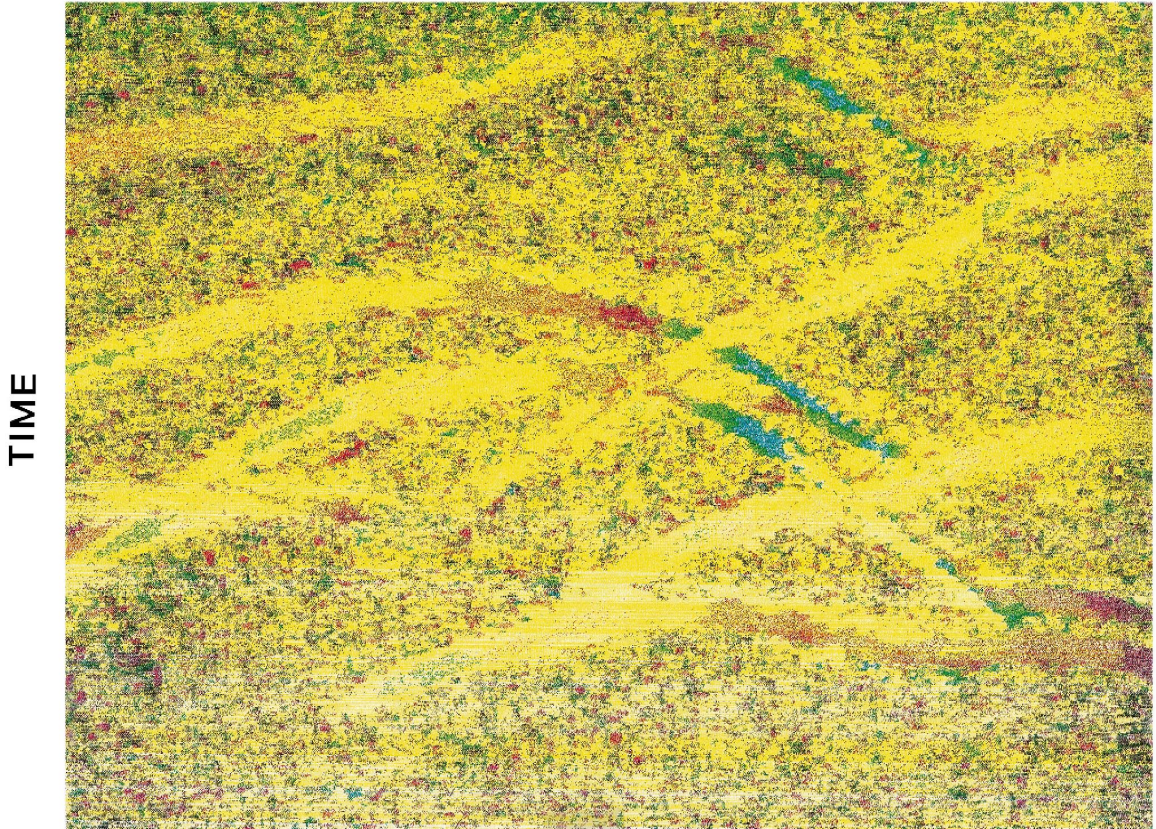


Fig. 30. CEE radiusgram.

the geometrical parameters of the front and the velocity near the seismic (reference) line. Assuming a spherical approximation for both cross-sections  $\Sigma_{ij}^-$  and  $\Sigma_{ij}^+$  and a constant velocity near the seismic line within the range of the array, the time correction formula is obtained. For distinct end points, the parameters entering the expression are two velocities near the source and receiver locations, two angles (departure and arrival) and two pairs of dual curvatures of the tube's cross-sections at the end points of the central ray. The first four parameters are common for all traces; the pairs of dual curvatures are specific, as a rule, for the selected ray tube. Owing to the large number of parameters (in particular, the curvatures), this formula cannot be used directly for practical applications.

For practical application, the family of dual curvatures is parameterized in two steps. In the first step, the exact formula for these curvatures is developed on the fixed central ray. It involves a pair of the dual curvatures of the selected fundamental ray tubes; thus, a pair of dual curvatures for any ray tube can be found using a pair of fundamental dual curvatures. In the second stage, the formula obtained is continued in the neighborhood of the central ray. The following scheme of time correction calculation is proposed: Let the zero-offset central point  $A_0(x_0)$  be fixed (Fig. 35). The neighborhood of the point  $A_0$  could then be presented in the form of a rectangle  $A_0KBEDLA_0$  in the acquisition plane. A point  $(X_s, X_r)$  in this plane has as coordinates source and receiver position, respectively.

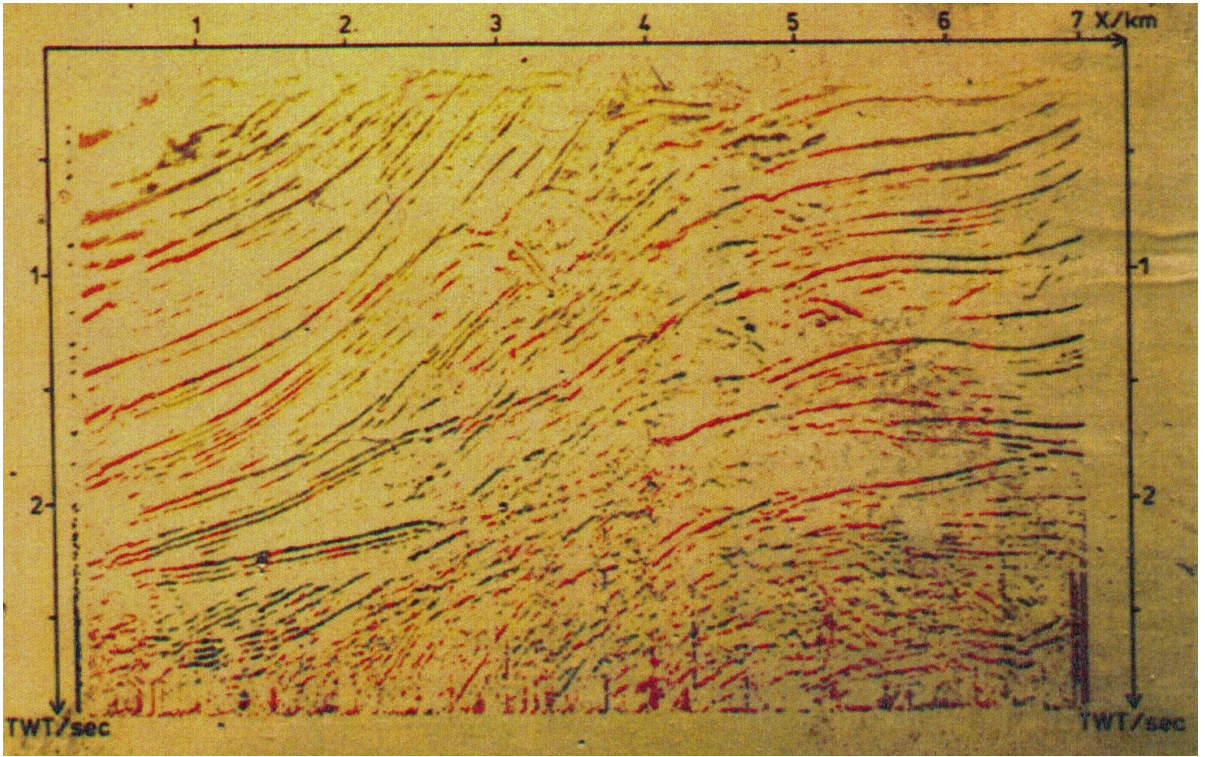


Fig. 31. CRE combined wavefield and anglegram time sections for the Marmousi model. By courtesy of W. Rabbel.

Choose a normalized trace  $\cos \varphi (x_s = x_0 + \Delta x_j^-, x_r = x_0 + \Delta x_i^+, t)$  from the rectangle vicinity. One must find the time correction  $\Delta\tau_{ij}$  for this trace with respect to the central trace.

If the angle of emergence  $\beta_0$  and the curvatures of the CRE and CEE fronts at point  $A_0$  are known, the dual curvatures and of the departing and arriving fronts (Fig. 34) can be calculated according to the relations:

$$k_{ij}^- = \frac{(k_{cee} + k_{cre})\Delta x_i^+ + (k_{cee} - k_{cre})\Delta x_j^- + 2 \sin \beta_0 k_{cee} k_{cre} \Delta x_i^+ \Delta x_j^-}{2\Delta x_i^+ (1 + \sin \beta_0 k_{cre} \Delta x_j^-)} \quad (20)$$

$$k_{ij}^+ = \frac{(k_{cee} - k_{cre})\Delta x_i^+ + (k_{cee} + k_{cre})\Delta x_j^- + 2 \sin \beta_0 k_{cee} k_{cre} \Delta x_i^+ \Delta x_j^-}{2\Delta x_j^- (1 + \sin \beta_0 k_{cre} \Delta x_i^+)} \quad (21)$$

From the dual curvatures for the ray tube  $T_{ij}$ , one gets the time correction according to the:

$$\Delta\tau_{ij} = \Delta\tau_{ij}^- + \Delta\tau_{ij}^+ \quad (22)$$

where

$$\Delta\tau_{ij}^- = \left[ \left( 1 + 2 \sin \beta_0 k_{ij}^- \Delta x_j^- + (k_{ij}^- \Delta x_j^-)^2 \right)^{1/2} - 1 \right] / k_{ij}^- v_0 \quad (23)$$

and

$$\Delta\tau_{ij}^+ = \left[ \left( 1 + 2 \sin \beta_0 k_{ij}^+ \Delta x_j^+ + (k_{ij}^+ \Delta x_j^+)^2 \right)^{1/2} - 1 \right] / k_{ij}^+ v_0 \quad (24)$$

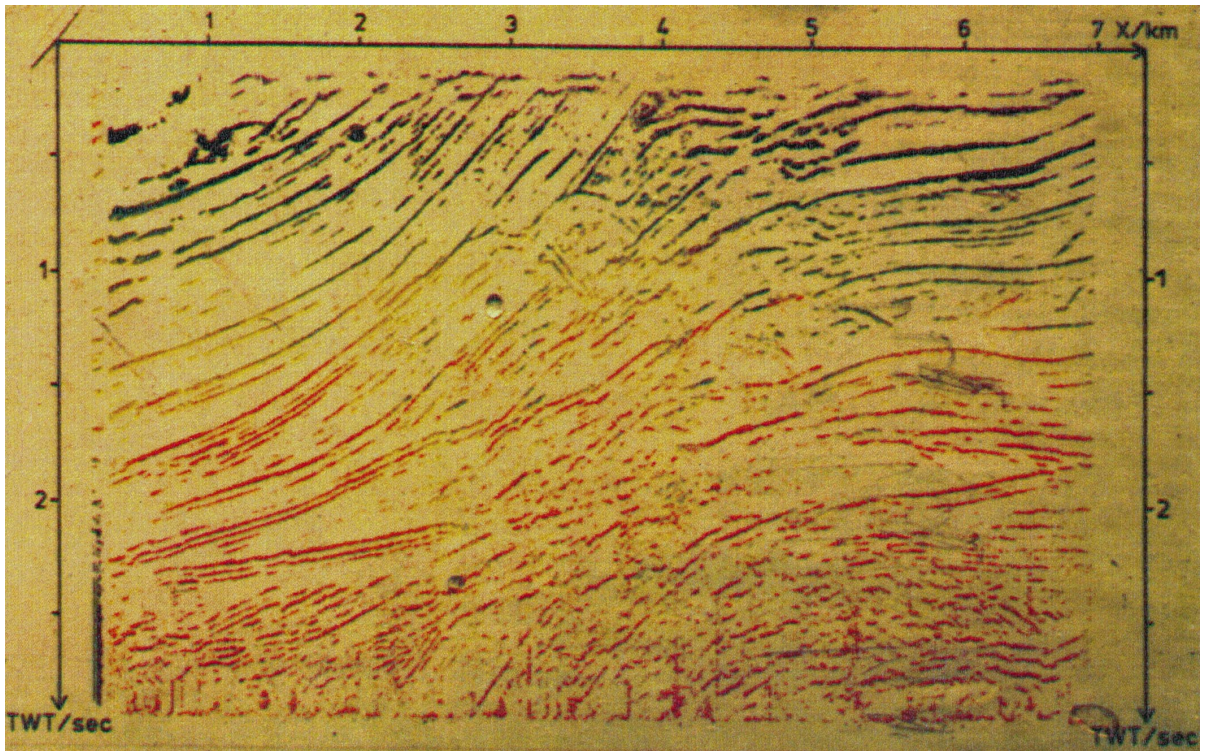


Fig. 32. CRE combined wavefield and radiusgram time sections for Marmousi model. By courtesy of W. Rabbel.

Now, the corrected normalized trace  $\cos \varphi (\Delta x_j^-, \Delta x_i^+, t_0 + \Delta \tau_{ij})$  where  $t_0$  is a time on the central trace can be found.

In the next step, another recorded trace with coordinates inside the rectangle  $A_0KBEDLA_0$  (Fig. 35) is selected and the corresponding corrected normalized trace is determined. In this way, all traces with coordinates located inside the rectangle can be corrected and a correlation criterion (i.e., semblance) calculated for a gather of corrected normalized traces. By changing the parameters (velocity, angle of arrival, and CEE and CRE curvatures) according to a systematic scheme or an optimization method allows to find the optimal time sections of the five types.

The term “multifocusing” has been chosen for the following reason (as shown above, see Gelchinsky et al., 2000b): the correction followed by stack of each normalized trace is equivalent to the focusing of the normalized field at some point located on the central ray or its continuation. Similarly, multifocusing processing can be interpreted as if the traces belonging to the vicinity of the fixed central ray were focused at many points, each trace to a distinct focus. For some HI schemes such as CRE and CSP, the focusing points can coincide.

There is a time correction formula applicable to small offsets known as the “combined CO and CMP approximation of NMO” (Gelchinsky et al., 2000b). In the “midpoint offset coordinate system”

$$y_{ij} = (\Delta x_i^+ - \Delta x_j^-) / 2 = (x_i^+ - x_j^-) / 2 \quad (25)$$

and

$$z_{ij} = (\Delta x_i^+ + \Delta x_j^-) / 2 = (x_i^+ + x_j^-) / 2 - x_0 \quad (26)$$

the time correction formula can be written as:

$$\Delta\tau_{ij} = \Delta\tau_{ij}^{\text{co}} + \Delta\tau_{ij}^{\text{cmp}}, \quad (27)$$

where

$$\Delta\tau_{ij}^{\text{co}} = (4 \sin \beta_0 z_{ij} + \cos^2 \beta_0 k_{\text{cee}} z_{ij}^2) / 2v_0 \quad (28)$$

and

$$\Delta\tau_{ij}^{\text{cmp}} = \cos^2 \beta_0 k_{\text{cre}} y_{ij}^2 / 2v_0. \quad (29)$$

For  $y_{ij} = 0$ , the first term in Eq. (27) is equal to the common offset (CO) or CEE time correction. Similarly, for  $z_{ij} = 0$ , the second term in Eq. (27) is equal to the CMP time correction. Thus, Eqs. (27)–(29) are applicable not only for the CO and CMP configurations, but also for arbitrary distribution of source–receiver pairs with small offsets. Here, only one example is given. Figs. 36 and 37 show the five time sections obtained by the different processing techniques. They are seismic images of the structure near a salt dome flank located in the Barents Sea. Comparison of conventional CMP and time migrated sections (Fig. 36a,b) with CEE and multifocusing time sections (Fig. 37a,b) shows that each can be divided into three clearly distinguished domains: the first domain with smooth, gently sloping reflectors corresponds to the sedimentary beds; the second domain is a transition zone represented by a bundle of steeply rising reflectors. The image of the salt dome flank, which is the target of this exploration, is situated in the transition zone. The third domain is the image of the salt dome. Only the upper part of the first domain appears similar on both CMP and CEE time sections; all other parts of the conventional and HI time sections are significantly different.

The sequence of phase lineups resembling reflections dipping smoothly towards the salt dome can be clearly seen on the stacked CMP time section in the first domain until about 4.0 s. These gently sloping lineups are crossed by the steeply rising lineups of the flank image in the second domain. On the stacked section (Fig. 36a), it is impossible to join dipping and rising lineups into continuous curves. On the migrated section (Fig. 36b), the conjugation of lineups is smooth but these joint areas move inside the salt dome as the recording time increases. Thus, the dome flank is less clear on the migrated section than on the CMP stacked section and, as a result, the dome flank, which can be associated with these joint points, can be roughly traced inside a zone about 1.3–1.6 km wide. The images of the salt dome (third area) and its flank (transition zone) are essentially different on the conventional sections (Fig. 36a and b) and on the CEE section (Fig. 37a).

The sea-bottom and near-bottom reflections can be traced only in the third domain on the CMP and migrated sections. Below them chaotic images are seen on Fig. 36a and b. Several additional, almost horizontal, lineups are seen in the salt dome area. These can be traced in the first area and, no doubt, they correspond to surface multiples of the sea bottom. These lineups should be suppressed by the CMP processing (using the  $fk$  multiple attenuation). However, the lineups identified in the first domain as multiples on the CEE stacked section are observed on the CMP section in the same domain, but not in the salt dome area. There is thus reason to assert that the  $fk$  multiple attenuation completely destroyed the multiple in the third domain but was not able to do so in the first domain, where bedding is far from quiet horizontal stratification.

Essential differences are observed between the images of the transition zone (second domain) on the CMP and CEE time sections, respectively. As previously stated, the gentle sloping and the steep lineups have acute intersections and could not be joined to continuous curves on the CMP section. On the CEE section, on the other hand, almost all the steeply rising lineups join the gentle sloping lineups

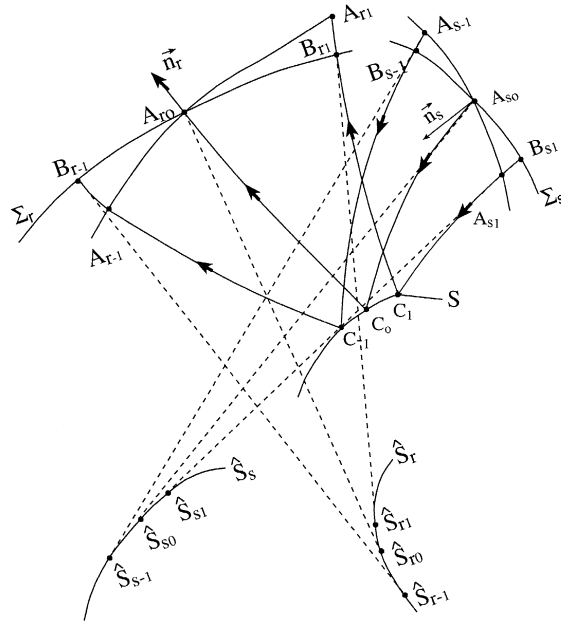


Fig. 33. Ray scheme of the homeomorphic imaging for a source–receiver distribution along two smooth curves located in a vertical plane and associated with two fictitious fronts.  $A_{s-1}A_{s0}A_{s+1}$  is the source line,  $A_{r-1}A_{r0}A_{r+1}$  is the receiver line;  $S$  is the element of the reflector;  $C_{-1}, C_0, C_1$  are reflection points;  $A_{s0}C_0A_{r0}$  is the central trace;  $\Sigma_s$  and  $\Sigma_r$  are, respectively, the wave fronts associated with sources and receivers;  $\hat{S}_s$  and  $\hat{S}_r$  are, respectively, the elements of the caustic of the front  $\Sigma_s(\Sigma_r)$  or the source (receiver) image of the reflector element  $S$ .

smoothly. The conjugations of several (at least four) take the shape of triplication arrivals having approximately the same horizontal coordinate.

Analysis of all four types of CEE sections, namely, time, anglegram, radiusgram and semblance-gram sections, lead the authors to conclude that only the four lineups marked in different colors on Fig. 37c (in green, yellow, blue, and red) could be identified with primaries with a high degree of accuracy. The deepest red wave is recorded in the first domain in the 1.5–1.65 s interval. The other lineups are peg–leg multiples. At least four loops on high order peg–leg multiple from the red interface can be seen. Three additional loop may be distinguished using a more careful examination of Fig. 37c. Hence, the seven loops, of which six may correspond to the multiples of the red wave, can be seen. It is perhaps more accurate to say that wave fields of these loops are heavily contaminated by multiples.

This conclusion means, in fact, that the salt dome flank and traces on the CMP, migrated and CEE time sections cannot be identified. This gives rise to a crucial problem: how should data processing be organized in order to trace the dome flank and map reflections below the red reflector? One possible way is to use a technique which suppresses multiples. A special HI technique has been developed for this purpose (Keydar et al., 1998), but is not discussed in this paper. However, this technique, like other methods of multiple suppression, can significantly deform primaries. Therefore, a new technique known as CSDE was used to trace the dome flank. This method is intended to pick out scattered and diffracted waves from a recorded total field (Gelchinsky et al., 1993). The CSDE method is based on the assumption that the flank of the salt dome could be considered a fractal surface. A modeling simulation of wave propagation in a medium with a fractal interface shows that after an incidence wave reaches this interface, a system of effective centers of diffraction (scattering) is formed in an

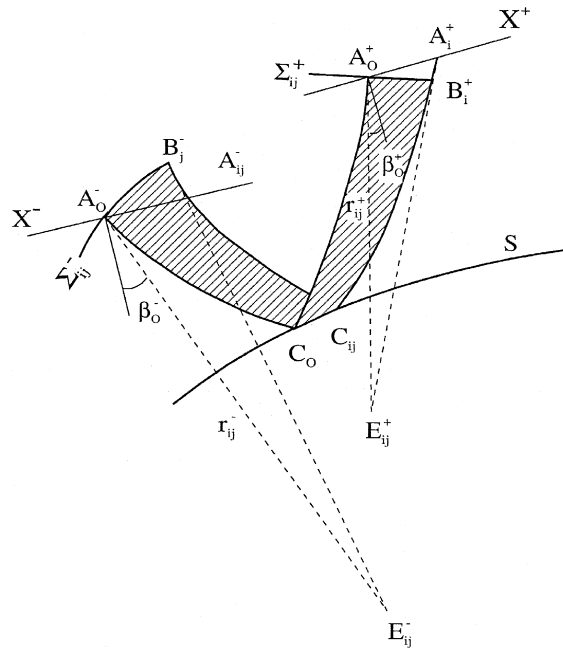


Fig. 34. Ray scheme illustrating association of a pair of traces with a ray tube. The line  $A_0^- C_0 A_0^+$  is the central ray corresponding to the trace  $u(A_0^-, A_0^+)$ , the line  $A_j^- C_{ij} A_j^+$  is the moving ray corresponding to the trace  $(A_j^-, A_j^+)$ ; the arcs  $A_0^- B_j^-$  and  $A_0^+ B_j^+$  are, respectively, the elements of the fronts  $\Sigma_{ij}^-$  and  $\Sigma_{ij}^+$  that leave (reach) the points  $A_0^-$  and  $A_0^+$ ; the dashed region  $A_0^- C_0 A_0^+ B_j^+ C_{ij} B_j^- A_0^-$  is the ray tube  $T_{ij}$  associated with the two traces;  $\beta_0^-$  and  $\beta_0^+$  are the angles of emergence and departure, respectively;  $r_{ij}^-$  and  $r_{ij}^+$  are the radii of curvature of the fronts  $\Sigma_{ij}^-$  and  $\Sigma_{ij}^+$ , respectively.

effective zone located around a fractal axis (Wainstein et al., 1992). Each center emits diffracted waves and, thus, a fractal interface can be considered a carrier of effective diffraction elements which

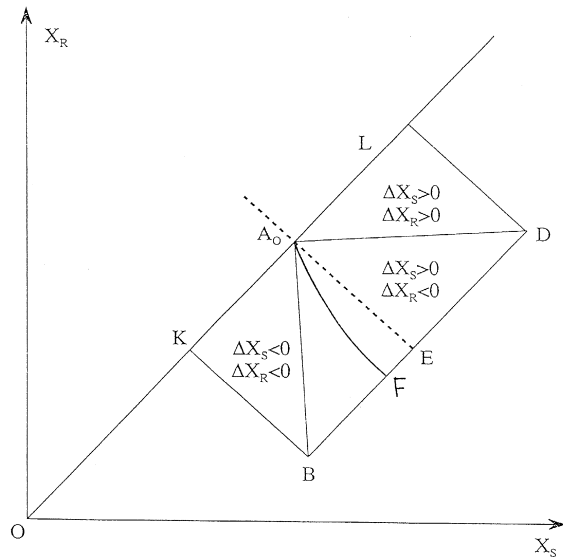


Fig. 35. Multifocusing stacking chart. The axes  $X_s$  and  $X_r$  are, respectively, source and receiver position;  $A_0$  is the central point; the rectangle  $A_0KBEDLA_0$  is the neighborhood of the point  $A_0$ ; the line  $OKA_0L$  is the CEE line, the line  $A_0E$  (or  $A_0F$ ) is the CMP (or CRE) line.

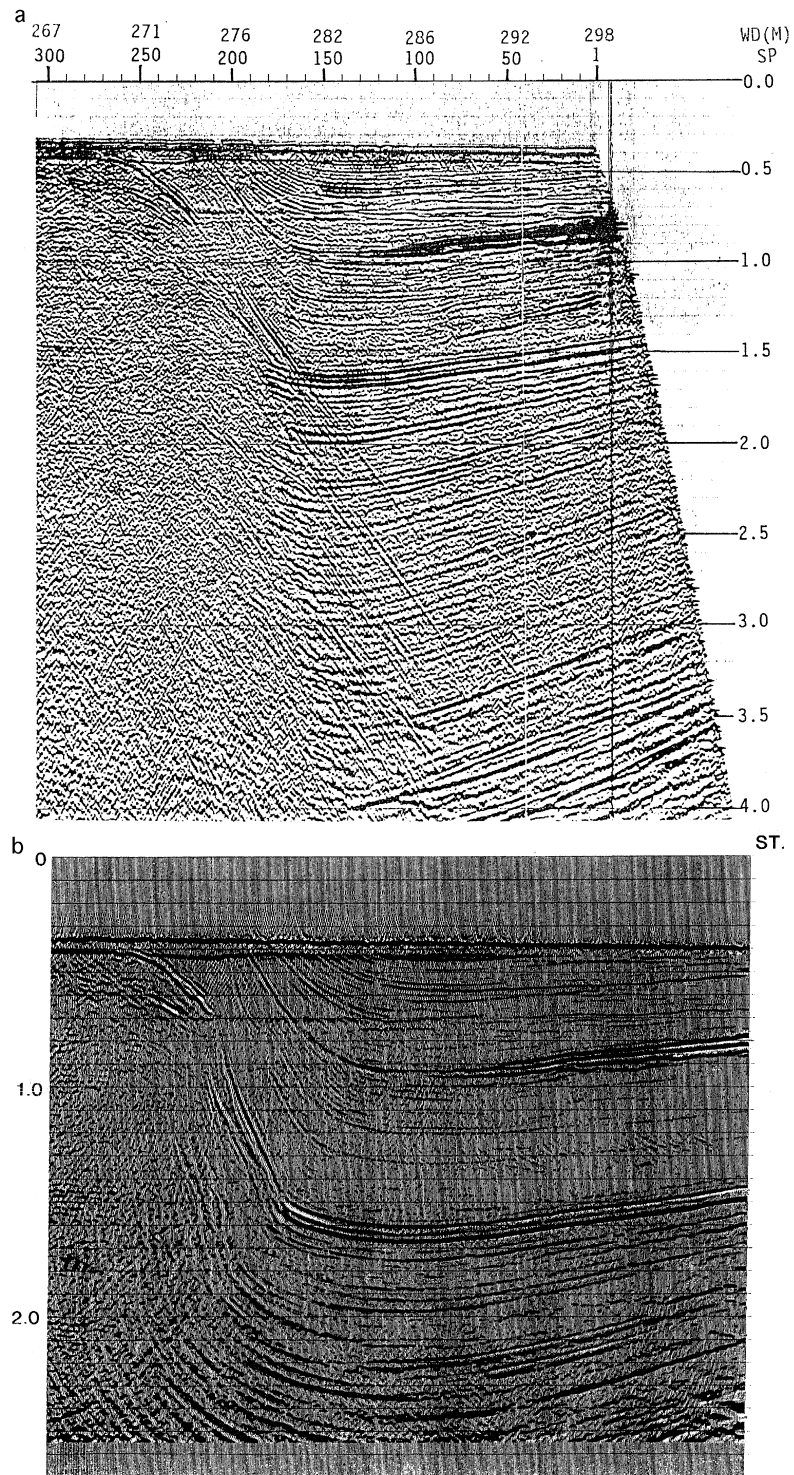


Fig. 36. (a) CMP stacked section. (b) Migrated section.

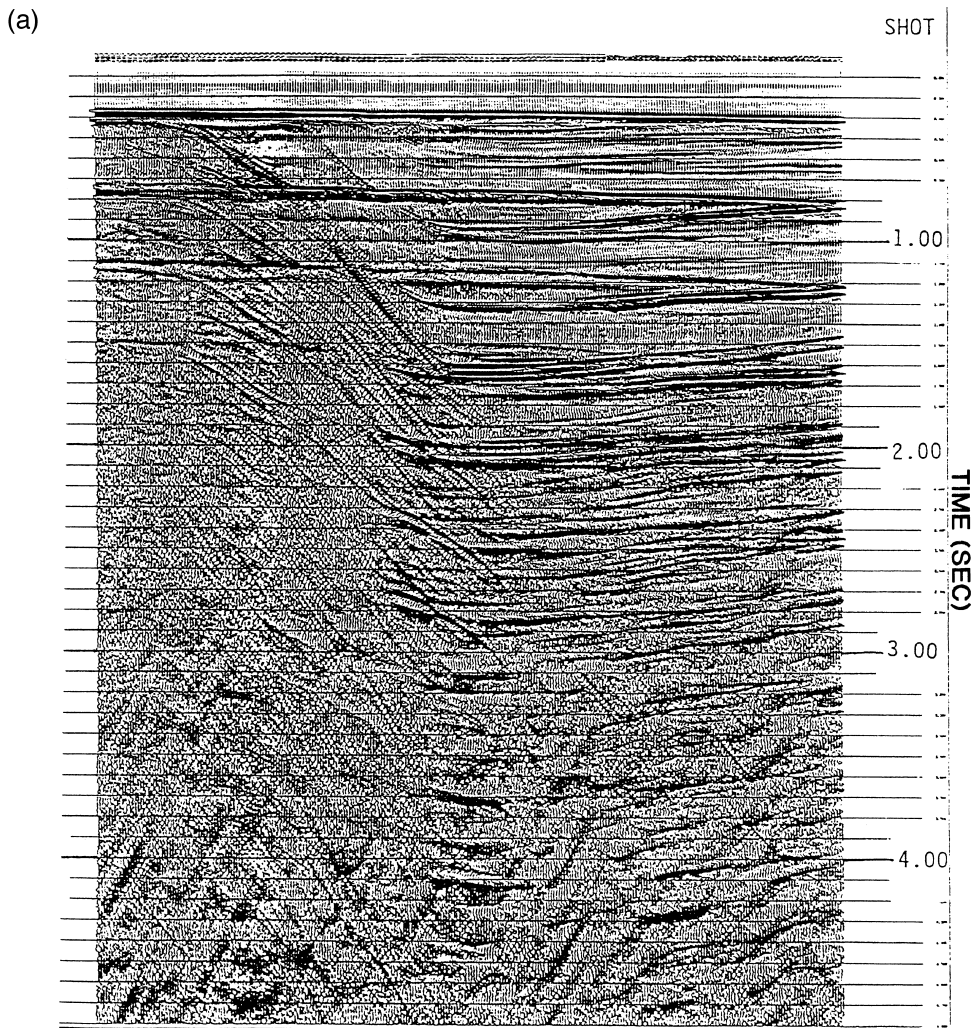


Fig. 37. (a) CEE stacked section. (b) Multifocusing stacked section. (c) CEE stacked section with picked primaries.

emit more and more diffraction waves as an incident wave propagates along the fractal. The CSDE method detects these diffracted waves.

Fig. 38a,b shows the so-called diffraction image semblancegrams. The abscissa corresponds to the location of a center of curvature of a diffracted waves, and the ordinate to two-way time from a diffraction center along a vertical path. The colors on these figures correspond to semblance. Only semblance values above a threshold are shown.

Some 800–900 traces were collected on one diffraction array, the semblance mean was 0.02–0.03 and the threshold was assumed equal to 0.1, i.e., three to four times the mean value. Fig. 38a (b) corresponds to a positive and a negative half plane. Positive half plane means the center of diffraction wavefront in  $x$ - $z$  space is below the earth surface and negative half plane means the center of diffraction wavefront in  $x$ - $z$  space is above the earth surface (Gelchinsky et al., 1992).

The main feature of diffraction image semblancegrams is that the spots of positions of high semblance values are located in a very restricted area. This means that the very strong field of

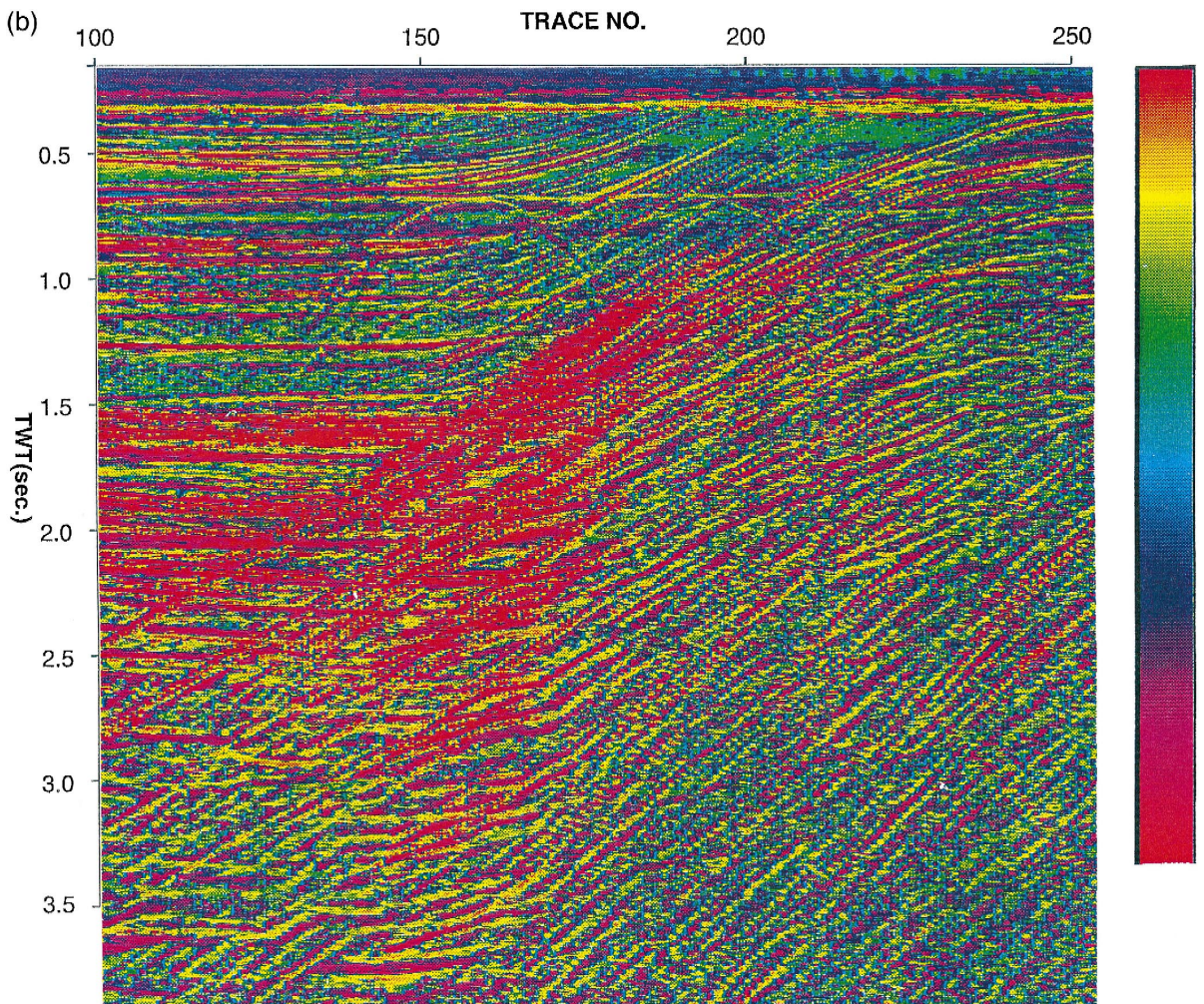


Fig. 37 (continued).

reflected waves is suppressed by the CSDE processing and the strip of spot locations, as the image of the salt dome flank, needs further consideration. This image can be clearly divided into two parts of polychromatic spots: the first corresponding to a cap rock of the salt dome, and the second to an almost vertical strip. Another essential peculiarity the picture in Fig. 38a is the presence of a shadow area dividing the two parts under consideration. It is very likely that this area is the image of a neck of the salt dome. The presence of the flank image in the negative image half plane (Fig. 38b) supports the theoretical expectation regarding the formation of two images of the dome flank in the positive and negative half planes, if the medium surrounding the dome flanks is inhomogeneous (Gelchinsky et al., 1992).

There is an additional feature of the flank image obtained: the hanging boundary located in the lower part of the cap rock image at time 800–1000 ms and between traces 205 and 280. It is appropriate to draw attention to the fact that the flank is mapped on very small distances (about 0.8–1.2 km). The main reason for recording waves at such short distances is the scattering by fractal

(c)

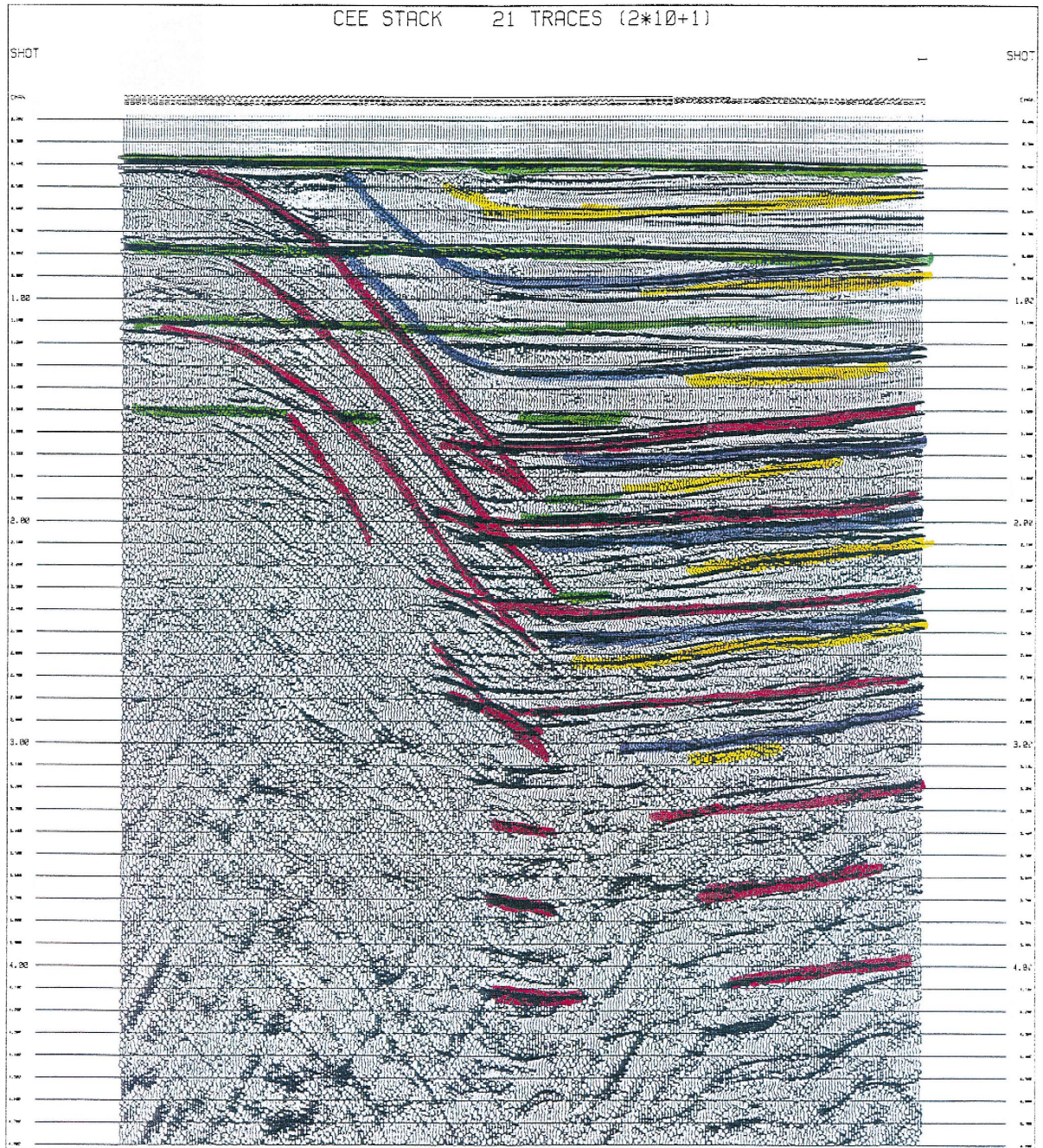


Fig. 37 (continued).

interface. Owing to the existence of a velocity gradient, it is possible to map the hanging part of the salt dome at small distances.

## 7. Solution of kinematic inverse problems

The output of HI correlation and decomposition is an optimally stacked time section  $u(x, t)$  as a function of coordinate  $x$  of a central point and zero time  $t$ , and the collection of parameter curves determined at each central point  $x_k$  ( $k = 1, 2, \dots, K$ ) for the  $m$ th lineup found ( $m = 1, 2, \dots, M$ ). This collection is formed by the travel times  $t_m(x) \rightarrow t_{km}$ , the angles of entry  $\beta(x, t) \rightarrow \beta_{km}$ , and the CRE and CEE radii  $r_{cre}(x, t) \rightarrow r_{km}$  and  $\rho_{cee}(x, t) = \rho(x, t) \rightarrow \rho_{km}$ . The parameters characterize the central rays and the dual wavefront elements of the ray tube at the end point of each ray. The values of these parameters for each ray depend on the structure of the medium in the illuminated area (the ray tube surrounding the central ray). This is the basis for solving the local kinematic inverse problem.

The first preparatory step in the solution of the inverse problem is the determination of the sequence of the detected events by decomposition of the optimally stacked sections. Corrections can be made by analyzing the wave picture in “the whole” after the results of the decomposition are available. Before solving the inverse problem, however, some constraints on the solution have to be introduced, since an unconstrained solution might require an unlimited number of parameters. These constraints take the form of assumptions regarding the type of structure. The inverse problem can then be parameterized and its solution is reduced to the determination of these parameters.

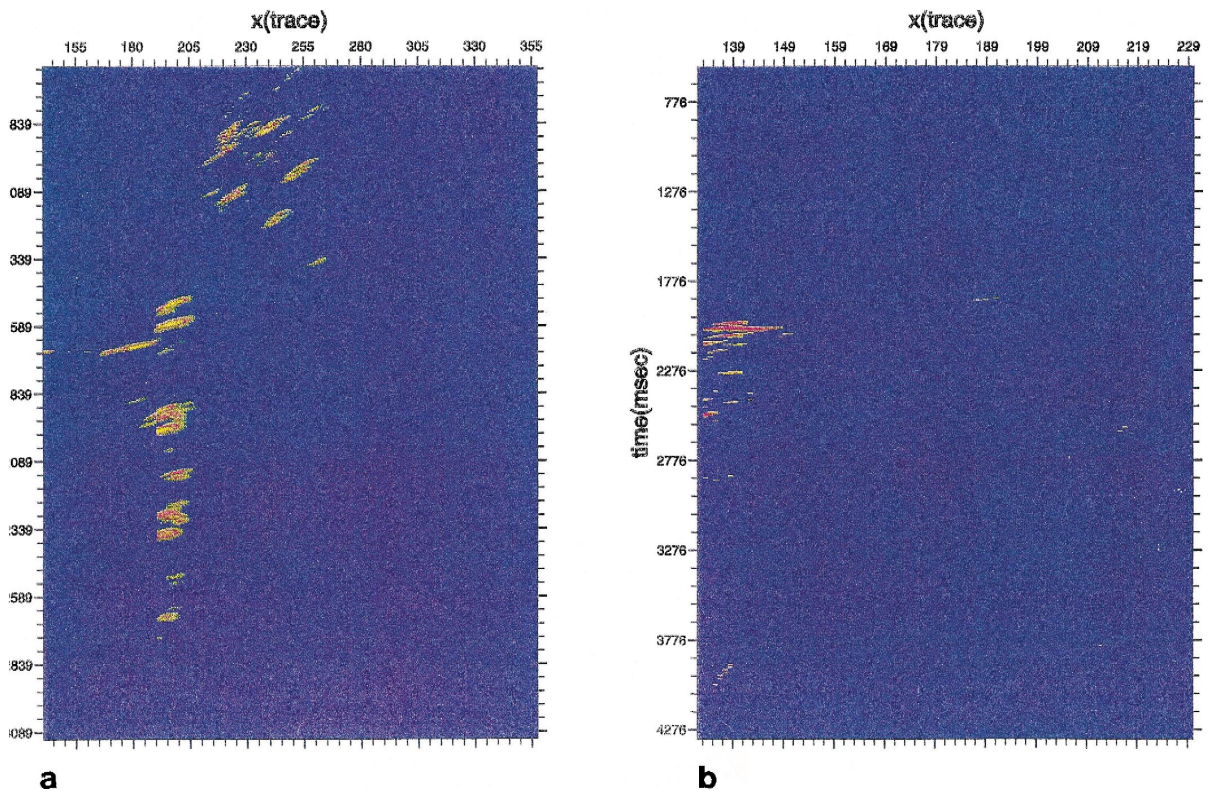


Fig. 38. Diffraction image semblancegram. The axis corresponds to the horizontal coordinate of a center curvature of a diffracted wave; the vertical axis is the two-way time  $t$  from a diffraction center to its projection on the surface. The color indicates semblance. The aperture for semblance estimation was 800 traces. The mean value of semblance was 0.02–0.03. Semblance values higher than 0.1 are shown in the figure. (a) Time image corresponds to positive depth of center of diffracted wave front. (b) Time image corresponds to negative depth of center of diffracted wave front.

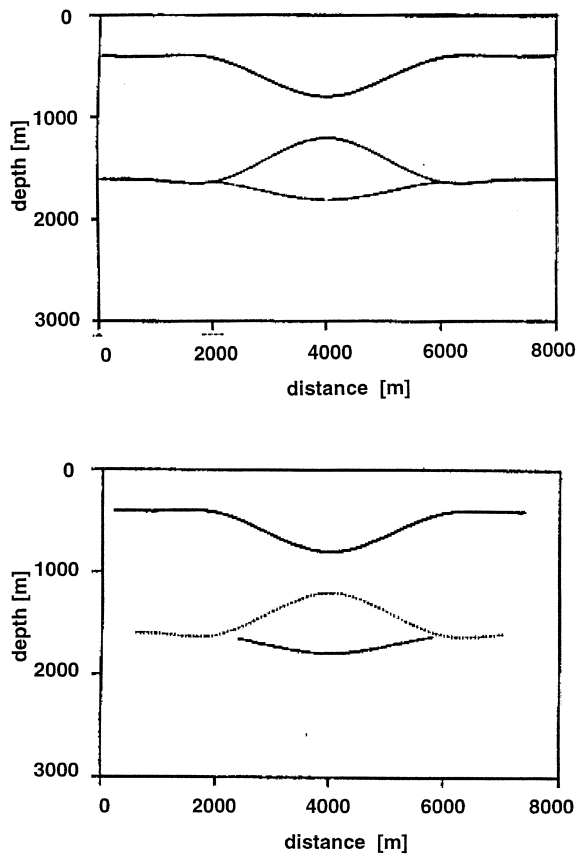


Fig. 39. (a) Input model. (b) Model obtained from the solution of inverse problem.

Note that the correlation procedure, optimal stack and construction of various types of images in HI processing do not require any assumptions regarding the type of structure. The constraints required for the solution of the inverse problem may make the region of applicability narrower than that of HI. It may be necessary in the solution of the inverse problem to test different constraints.

As usual, the most important constraint refers to the velocity of wave propagation. The velocity structure of each layer — the part of the medium located between two subsequent curvilinear interfaces — is parameterized. It is assumed that the velocity distribution  $v(x, z)$  in the  $m$ th layer is described by the relation:

$$v_m(x, z) = \phi(x, z; a_{0n}, a_{1n}, \dots, a_{Qn}) \tag{30}$$

where  $\phi$  is a function of a fixed type and  $a_{0m}, a_{1m}, \dots, a_{Qm}$  are the parameters of  $\phi$  for the  $m$ th layer. In Berkovitch and Gelchinsky (1989) and Keydar et al. (1996), the polynomial

$$v_m(z) = a_{0m} + a_{1m}z + \dots + a_{Qm}z^Q \tag{31}$$

is used.

As is usual in local methods, description of interfaces is linked to the rays. The horizontal and vertical coordinates  $\xi_{km}$  and  $\zeta_{km}$  of the points  $C_{km}$  of the intersection of central ray  $A_k C_{km}$  with the  $m$ th reflector, the dip angle  $\varphi_{km}$  and the radius of curvature  $R_{km}$  of the  $m$ th interface at point  $C_{km}$  are chosen as parameters for the reflector. Thus, each interface is regarded as a carrier of curvilinear

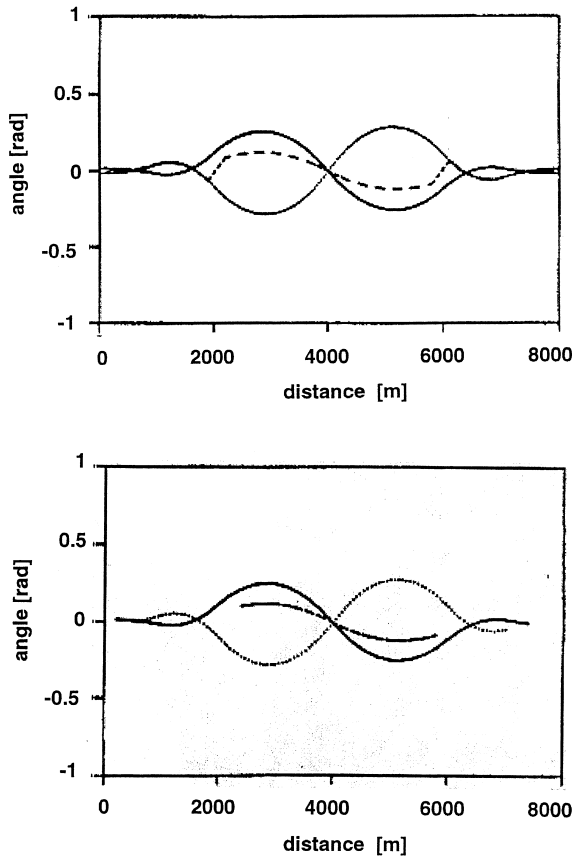


Fig. 40. (a) True normal angles of the reflectors forming the model. (b) Normal angles obtained from the solution of inverse problem.

elements, each characterized by the central point  $C_{km}$  with coordinates  $\xi_{km}, \zeta_{km}$ , the angle  $\varphi_{km}$  between the normal and the vertical, and the radius of curvature  $R_{km}$ . In the solution of the inverse problem, a group of these elements situated between critical points can be considered part of a smooth reflector, and a united solution for the corresponding group of rays is constructed. The aim of the local kinematic inverse problem is, therefore, to find the coordinates  $\xi_{km}, \zeta_{km}$ , the angles  $\varphi_{km}$  and the radii  $R_{km}$  at each point  $x_k$  ( $k = 1, 2, \dots, K$ ) of each interfaces ( $m = 1, 2, \dots, M$ ) and the velocity parameters  $a_{qm}$  ( $q = 1, 2, \dots, Q$ ) for each layer. The solution of the inverse problem should satisfy the ray tracing system

$$\begin{aligned} \frac{dx_i}{dt} &= v^2 p_i, \\ \frac{dp_i}{dt} &= \frac{d}{dx} \ln v, \quad i = 1, 2, \end{aligned} \tag{32}$$

combined with the equation for the radius of curvature of the wave front

$$\frac{dr}{dt} = v - v_s r + v_{nm} r^2, \tag{33}$$

where  $x_1$  and  $p_1$  are the horizontal and  $x_2$  and  $p_2$  are the vertical projections of a ray trajectory and the slowness vector  $p$ , respectively;  $v_s$  is the first derivative of the velocity  $v$  along the tangent  $s$  to a

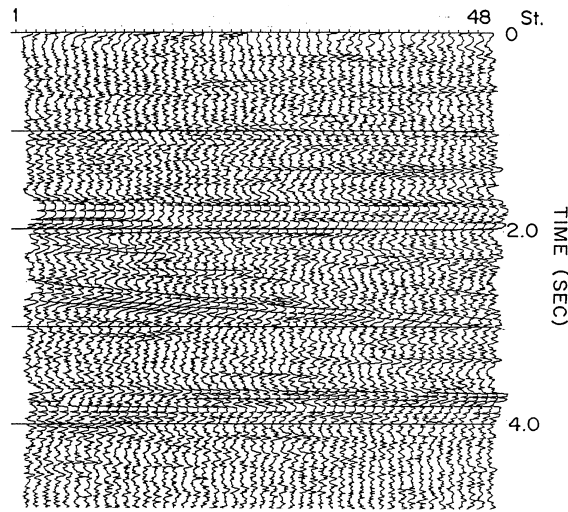


Fig. 41. Semblancegram of combined HI processing for the data shown in Fig. 24.

ray,  $v_{nn}$  is the second derivative of the velocity  $v$  along the normal  $n$  of a ray, and  $r$  is the radius of curvature of the wavefront at a point  $(x, z)$ . The initial conditions for systems (32), (33) and the  $m$ th reflection event are:

$$z = 0, \quad x = x_k, \quad t = t_{km}, \quad p_1 = \sin \beta_{km}/v_0, \quad p_2 = \cos \beta_{km}/v_0, \quad r = r_k,$$

or

$$r = \rho_{km} \tag{34}$$

where  $v_0$  is the velocity near a seismic line or a reference level. As may be observed from the initial conditions, the two radii of front curvature (radii corresponding to the CRE and CEE ray tubes) are determined for each ray that is constructed.

The optimal velocity parameters  $\hat{a}_{qm}$  ( $q = 0, 1, \dots, Q$ ;  $m = 1, 2, \dots, M$ ) of layer  $m$  and the coordinates  $\xi_{km}, \zeta_{km}$  ( $k = 1, 2, \dots, K$ ), the angles  $\varphi_{km}$  and the radii  $R_{km}$  of the  $m$ th interface are found by the following recurrent optimization procedure. In the first cycle, the parameters related to the first layer and the first interface are determined. All characteristics  $x_{km}, t_{km}, \beta_{km}, r_{km}$  and  $\rho_{km}$  ( $m = 2, 3, \dots, M$ ) of the subsequent reflection events are reduced to the first interface found before the second cycle is entered. After determination of the parameters related to the second layer and interface, the third cycle begins, and so on.

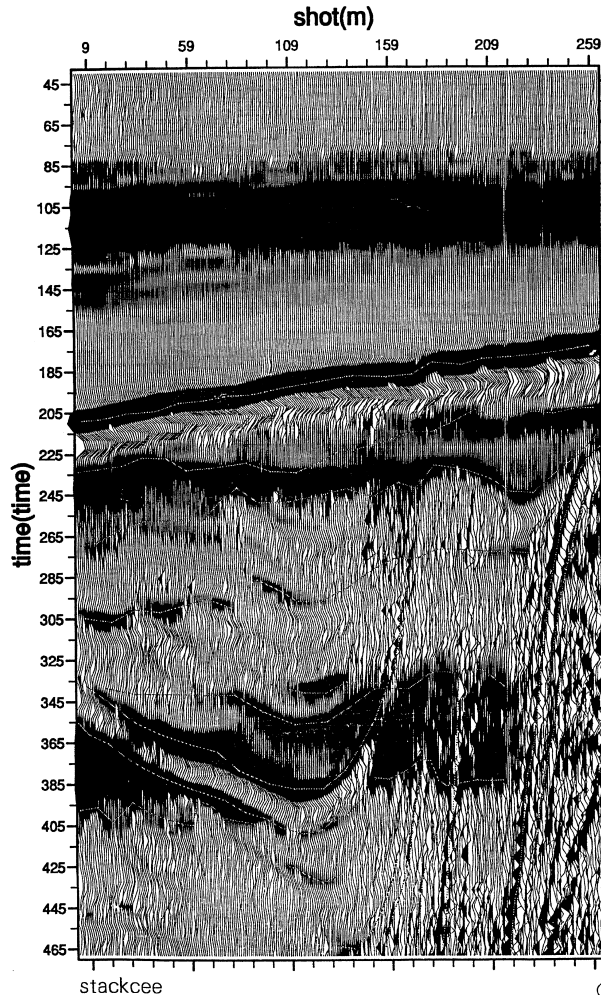
The search for optimal parameters in the  $m$ th cycle starts with the choice of an initial combination of the velocity parameters  $a_{qm}^1$  and the calculation of the ray trajectories for the  $m$ th reflection event propagating backwards from the interface  $m - 1$  to the  $m$ th reflector, which is reached at the instant  $t = 0$ . The coordinates  $\xi_{km}^1$  and  $\zeta_{km}^1$  and also the CRE radii  $r_{km}^1$  are determined for this instant for all rays of the set  $k_1 < k < k_2$  corresponding to the interval between the two critical points. After this, a new set of initial parameters  $a_{qm}^2$  is chosen and the coordinates  $\xi_{km}^2, \zeta_{km}^2$  and  $r_{km}^2$  are determined. This loop is repeated up to the  $s$ th combination  $a_{qm}^s$  of the velocity parameters has been selected and the coordinates  $\xi_{km}^s, \zeta_{km}^s$  and  $r_{km}^s$  of the  $m$ th have been determined.

The next step is the determination of the optimal  $\hat{a}_{km}$ ,  $\hat{\xi}_{km}$  and  $\hat{\zeta}_{km}$ . These are found by minimization of

$$\min_s \sum_{k_1}^{k_2} [r_{km}^s(a_{0m}^s, a_{1m}^s, \dots, a_{Qm}^s)]^2 = \sum_{k_1}^{k_2} \hat{r}_{km}^2(\hat{a}_{0m}, \hat{a}_{1m}, \dots, \hat{a}_{Qm}). \tag{35}$$

The optimal normal angle  $\hat{\varphi}_{km}$  and the optimal radius  $\hat{r}_{km}$  of reflector curvature are also found at each point  $\hat{S}_{km}$  with coordinates  $\hat{\xi}_{km}$  and  $\hat{\zeta}_{km}$  in the following way. The angle is determined by the tangent direction of the ray at its end point on the  $m$ th reflector. The optimal radius  $\hat{r}_{km}$  of reflector is equal to the CEE radius  $\hat{\rho}_{km}$  at the end point  $\hat{S}_{km}$ .

A continuous description of the  $m$ th reflector can be found in two ways. One can determine a spline (or other) approximation of a curve when the depth and the first two derivatives of the interface are given at a point having horizontal coordinate  $\hat{\xi}_{km}$ . This yields an equation of the form  $z_m = f(x)$  for



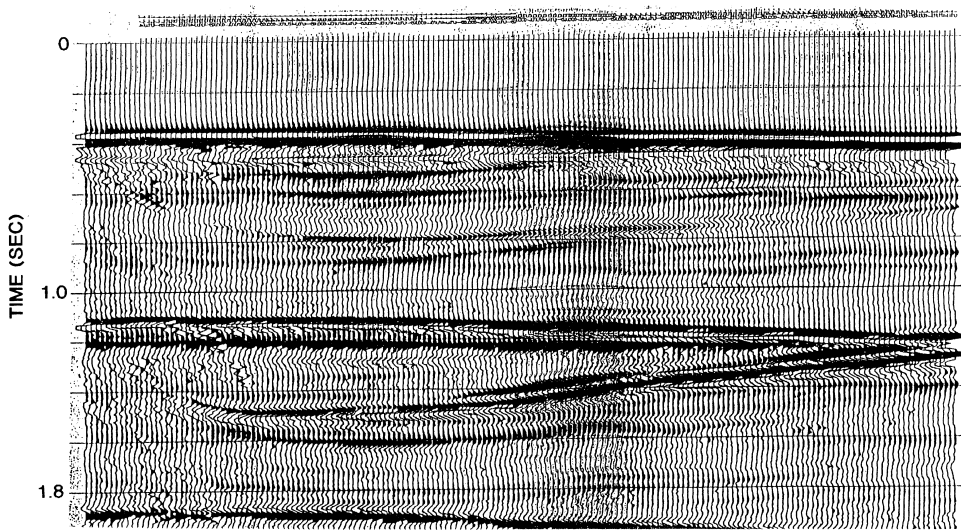


Fig. 42. CEE time sections illustrating the feasibility of the HI technique for stratigraphic studies, sequence analysis, etc. (a) Near see bottom (zoomed). (a) Time section corresponding to a gentle sloping bedding.

the  $m$ th reflector. The second version uses separate continuous approximations of depth points, normal angles and radii of curvature at these points. This yields the three equations

$$z_m = f_{z_m}(x) \quad \varphi_m = f_{\varphi_m}(x) \quad R_m = f_{R_m}(x) \quad (36)$$

for the  $m$ th interface. The sequence of the functions  $f_{z_m}(x)$  ( $f_{\varphi_m}(x)$  or  $f_{R_m}(x)$ ) for  $m = 1, 2, \dots, M$  is called the depth (angle or radius, respectively) model of interfaces.

For the descriptions by splines, numerical differentiations of the function  $f(x)$  is required. This is avoided in description (36). This has obvious advantages for ray construction and calculation of the radii of wavefront curvature, where angles of incidence and radii of surface curvature should be found at each point of intersection of the ray with intermediate interfaces. A simplified version of this approach was used by Berkovitch (1995), Berkovitch and Gelchinsky (1989), Berkovitch et al. (1991), and Keydar et al. (1995). An example follows below.

Figs. 39 and 40 speak for themselves. The depth and angle models fit the corresponding test models very well.

The problems in Figs. 39 and 40 were simplified: there was no noise, and the initial conditions were obtained by direct calculation. The purpose of these exercises was to test the methods of solution under simple, sterile conditions. Undoubtedly, noise, complex interfaces, and a larger number of critical points would destabilize the inverse solution unless the method is improved. There are several ways in which the method may be improved: utilization of output of different types of HI methods, accurate elimination of critical points in the solution scheme under discussion, use of different levels of model description for smooth parts of the interfaces and the application of results obtained using the multifocusing theory.

## 8. Combined interpretation of HI data

The interpretation of the diverse data obtained through HI processing is a promising subject, but no dedicated work has been done in this area, thus, only a fragmentary sketch of what has been obtained

and what could be achieved in the combined interpretation of HI data can be given. HI processing gives the following output:

- Stacked wavefield time section  $u(x, t)$
- Semblancegram  $S(x, t)$
- Anglegram  $\varphi(x, t)$
- CRE and CEE radiusgrams  $r(x, t)$  and  $\rho(x, t)$
- Arrival time  $t_m(x)$
- Angle of entry  $\beta_m(x)$
- CRE and CEE radii  $r_m(x)$  and  $\rho(x, t)$  curves
- Kinematic seismic model: functions  $v_m(x, z)$ ,  $a_m(x)$ ,  $\varphi_m(x)$  and  $R_m(x)$ , with  $m = 1, 2, \dots, M$

The time sections present the wavefield characteristics, while give geometrical attributes of wave fronts in the form of the 2D function of coordinates and time. These are independent and none can be obtained from the others by any manipulation. The parametric curves shown {in the third row} are not strictly independent from the anglegrams and radiusgrams, but the decomposition procedure includes informal operations so that for practical purposes the parametric curves may be considered as independent. Thus, the best way to extract the maximum information contained in the data set is through combined interpretation. However, there is not yet any theory of combined interpretation nor any experience.

The wavelets of different events on the HI stacked time sections have a much broader spectrum than that of seismic traces of corresponding gathers before stack. This could possibly be explained by the non-linearity of optimal HI stacking and/or by the sensitivity of optimal stacking to the stability of reflecting interfaces (thin layer packets) in a lateral direction. This phenomenon results in a substantial diversity of wave forms on the stacked HI time sections of real data, is not present on time sections of synthetic data from models with smooth interfaces.

The combined wavefield stacked time section in Fig. 24a and the corresponding combined semblancegram in Fig. 41 illustrate this phenomenon. Even at first glance, the great diversity of waveforms seen on the pictures and the substantial alteration in their apparent frequencies is obvious.

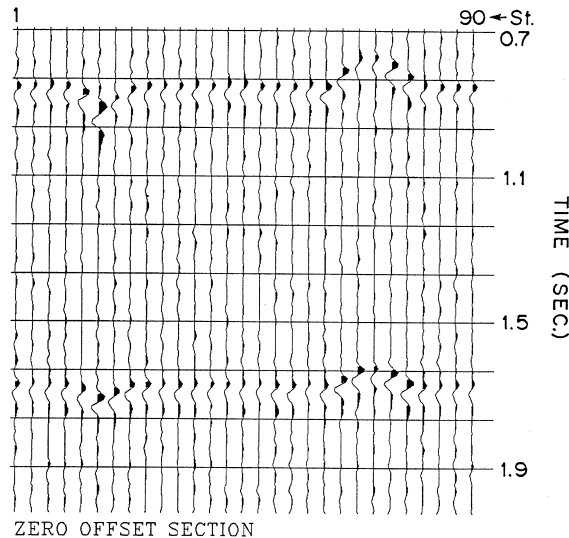


Fig. 43. Synthetic model with undulating interfaces. CEE stacked section.

It is possible to note that the apparent frequency of the fixed wave impulse may change significantly from one phase to another; waveforms of this type can be traced along the entire seismic line. In other cases, the wavelets change gradually from trace to trace. Further illustrations of this feature of HI stacked time sections are shown in Fig. 42a and b (Gelchinsky et al., 1992). The first corresponds to the upper part of sea bottom sediments and the other to deeper deposits. The complicated picture seen in Fig. 42 shows in detail the structure of the sea bottom in the studied area. In Fig. 42, a similar diversity of the waveforms as in Fig. 24 may be observed, but differing from it in its greater instability.

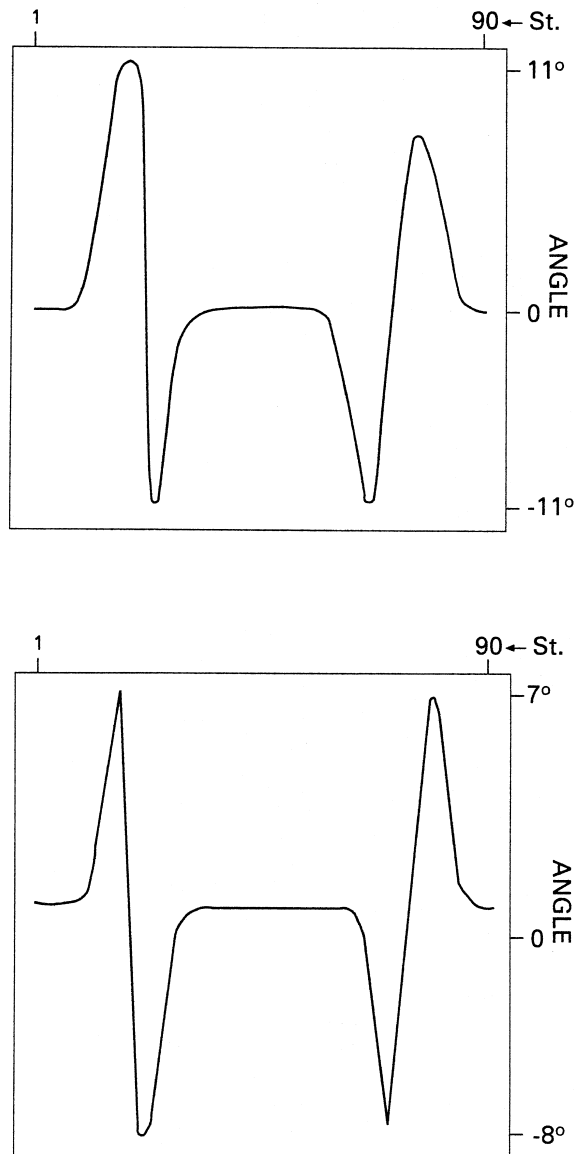
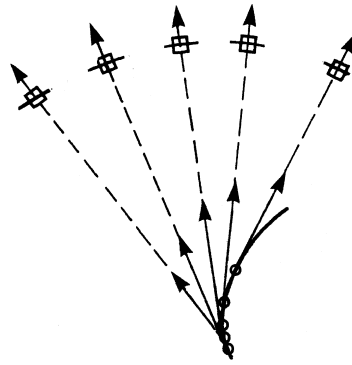
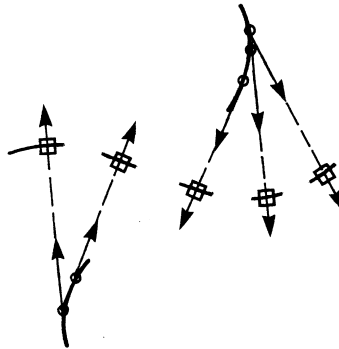


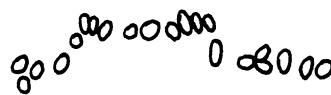
Fig. 44. (a) CEE angle curves for the first reflector of the model shown in Fig. 43. (b) CEE angle curves for the second reflector of the model shown in Fig. 43.



(a)



(b)



(c)

Fig. 45. Three types of interfaces and their CRE shown by squares and CEE shown by circles images: (a) smooth reflector, (b) smoothly oscillating, (c) fractal scatterer.

Both the accuracy and resolution of the tracing procedure could be significantly improved if analysis of the anglegrams and radiusgrams is included. In this case, one could try to establish

relations between areas of waveform change and zone of wavefront attribute alterations. Examples of picking these zones were presented in the preceding sections. The features of HI discussed here could be applied for essential development of stratigraphic studies and sequence analysis.

We now turn our attention to the homeomorphic images and their projections. The theoretical basis of their direct use by interpretation is a consequence of the basic HI property, the conservation of critical points. A corresponding concept can be formulated in the following simplified form: a set of homeomorphisms (a manifold) described by a collection of its images (an atlas) is necessary for studying the geometrical and topological properties of an object (original), particularly for complex structures. An example of this concept is discussed in Section 3, i.e., the construction and study of patterns of critical points (portraits) in the HI space. Since detection of critical points and the study of their patterns is particularly difficult in a physical space owing to the complicated structure of the overburden, the exploration of possibilities for studying HI portraits for geological and engineering interpretations is one of the most interesting, difficult but promising problems in HI theory and practice.

We study an undulations with small amplitudes and large angles. The CEE time section is shown in Fig. 43. This picture reveals that detection of such undulation is very difficult, since they could be masked by noise, so that they are often below resolution of the seismic method. However, the angle curves in Fig. 44a and b clearly show the undulations. A similar picture is obtained for the radius curves. It should be pointed out that (a) the angle and radius curves are projections of the CEE homeomorphic image on the  $(x, \beta)$  and  $(x, r_0)$  planes, and (b) the angles and radii are obtained in HI processing as parameters and not by differentiation. Thus, this simple example illustrates that the study of atlases of homeomorphic images may sometimes provide better results than the study of the objects themselves.

The next example relates to the determination of the smoothness of interfaces forming reflected and/or diffracted (scattered) waves using combined CRE and CEE images. This problem is of theoretical and practical interest; for example, a reservoir surface, metamorphism front or fault plane, etc. could often be considered as a fractal surfaces. Without giving further details, we introduce the following three types of interface shown in Fig. 45: (a) a smooth reflector, (b) an interface with smooth undulations, and (c) a fractal-like interface. These types of interface can be recognized with the help of their combined CRE and CEE images, each of which may be found in the following way: the loci of the centers of curvature of the CRE and CEE fronts are constructed (squares for CRE image and circles for CEE images). These fronts correspond to reflection events for Fig. 45a and b and diffracted events for Fig. 45c. It may also be noted that the combined CRE and CEE images of these types of subsurface differ from each other substantially.

## 9. Conclusions

The future development of the HI approach will occur in three areas:

- present and future development of the HI technique and expansion of its applications,
- research problems connected with the creation and development of new HI methods, and
- problems of the creation, development and application of the combined interpretation of HI data.

At present, problems with the HI methods are mainly of a technological nature. The corresponding algorithms need to be improved, e.g., the correlation and stacking procedure should be optimized and the various HI methods should be integrated. Another important task is the development of a reliable algorithm for the decomposition.

Often a second stage of HI processing is desirable to improve resolution and extract more detailed information. This requires non-spherical approximation of wave fronts and a new approach to studies of critical points and their neighborhoods. One promising line of development is direct detection of angle points of interfaces and the determination of their location in the image plane. Similar methods for other types of critical points can be expected in the not too distant future.

An important task is the development of 3D HI methods. This is conceptually difficult, and requires careful matching of models and methods. The greatest practical problem with 3D processing is computing time. Only sophisticated hardware and well-designed algorithms can overcome this obstacle. However, it is expected that the advantages of the HI approach in 3D processing will be even more substantial than in 2D processing. A tremendous amount of information accumulated by 3D acquisition systems remains unutilized by conventional processing.

The structure and pattern of critical points could be studied in the HI approach at several levels.

- The first level corresponds to the time sections of all types which are the output of the correlation and stacking procedure. A rough qualitative interpretation could be carried out at this level.

- At the second level, the parametric curves, group homeomorphic image and a set of projections of different types of HI images are used as the basis of the combined interpretation. This is the most interesting stage because it is performed with enlarged portraits of critical points in 2D or 3D section (projections) of multidimensional space in which topologically deformed equivalent images are mapped. This stage appears to be the most convenient for the construction and study of the portraits.

- At the third level, the kinematic seismic model together with the migrated portraits of critical points obtained at the preceding stage undergo combined interpretation. All the structural characteristics found should be put in their places in the physical space. This is a major operation, but information missed at the second level cannot, apparently, be reconstituted later.

The combined interpretation at all levels should be carried out by a team of specialists in different fields (a geophysicist and a geologist at least). During the initial stages of geological and geophysical interpretation, the joint work of both specialists is absolutely necessary.

A unique aspect of the HI approach is that it works with topologically equivalent patterns of critical points in the image space instead of the pattern itself in the physical space. This is a completely new approach, not only in geophysics and geology, but also in many areas of science and industry. Interestingly, this theoretical approach appeared during the solution of another problem. This situation can be described by the penultimate sentence from the novel “*Wilhelm Meister’s Lehrjahre*” by Goethe: “You remind me of Saul, the son of Kis who went to look for his father’s she-asses and found a kingdom”. The situation is similar in our case, when searching for an independent time correction formula, the world of HI was found. There is also a difference between these situations, however, the HI world is different from the kingdom, which is a the guarded possession. The HI world is a public domain. Any open minded specialist with some imagination and good will can enter the world of HI, where he can make wonderful discoveries and grow fruit useful for himself and for his company. Welcome to the world of HI!

## **Acknowledgements**

One of the authors, Boris Gelchinsky, would like to bring his deep gratitude to the Alexander von Humboldt Foundation for support and creation of excellent condition for working and writing during his stay at Karlsruhe University. The work of Shemer Keydar was supported by the Earth Science

Research Administration of the Israel Ministry of Energy and Infrastructure and by the Geophysical Institute of Israel. The authors thank Prof. Peter Hubral for his interest in this work and for numerous fruitful discussions which had a great influence on this paper. We are grateful to Klaus Helbig for his exceptional review and extensive editing of the paper which improved its readability. The authors are grateful to Prof. Wolfgang Rabbel for supplying the CRE data for publication. We also thank Boris Gurevich for his helpful comments during the review.

## References

- Berkovitch, A., 1995. The multifocusing method for homeomorphic imaging and stacking of seismic data. PhD Thesis, Tel Aviv Univ.
- Berkovitch, A., Gelchinsky, B., 1989. Inverse of common reflecting element data. 59th Ann. Int. Mtg., Soc. Exp. Geophys., Expanded Abstracts, pp. 1250–1253.
- Berkovitch, A., Gelchinsky, B., Keydar, S., Shtivelman, V., 1991. Inversion of combined data of the CRE and CEE imaging (stacks). 53rd Mtg. and Tech. Exh., AO-23.
- Berkovitch, A., Gelchinsky, B., Keydar, S., 1994. Basic formulae for multifocusing stack. 56th Mtg. Eur. Assoc. Expl. Geophys., Extended Abstracts, Session, P140.
- Cerveny, V., 1985. The application of ray tracing to the numerical modeling of seismic wavefields in complex structures. In: Dohr, G. (Ed.), *SEISMIC SHEAR WAVES: Part A. Handbook of Geophysical Exploration*. Geophysical Press, pp. 1–124.
- Cerveny, V., 1987. Ray Method for Three- Dimensional Seismic Modeling; Petroleum Industrial Course. The Norwegian Institute of Technology, Trondheim.
- Cerveny, V., Ravindra, R., 1971. *THEORY OF SEISMIC HEADWAVES*, Toronto.
- Deregovsky, S., Rocca, F., 1981. Geometrical optics and wave theory for constant offset section in layered media. *Geophys. Prospect.* 29, 374–387.
- Dix, C.H., 1955. Seismic velocities from surface measurement. *Geophysics* 20, 68–86.
- Gelchinsky, B., 1988. Common reflecting element (CRE) method. *Explor. Geophys.* 19, 71–75.
- Gelchinsky, B., 1989. Homeomorphic imaging in processing of seismic data (fundamentals and schemes). 59th Ann. Intern. Mtg., Soc. Exp. Geophys., Expanded Abstracts, p. 59.
- Gelchinsky, B., Keydar, S., 1993. Basic HI formulas of general theory of local time correction. 63rd Ann. Intern., Soc. Exp. Geophys., Expanded Abstracts, pp. 1145–1148.
- Gelchinsky, B., Landa, E., Shtivelman, V., 1985. Algorithms of phase and group correlation. *Geophysics* 50, 596–608.
- Gelchinsky, B., Landa, E., Shtivelman, V., 1986. Complex envelope and procedures of combined group and phase correlation. 56th SEG, Expanded Abstracts, POS2.6.
- Gelchinsky, B., Keydar, S., Helle, H., 1992. Structural imaging of a salt dome by HI methods. *Seismo-Series*, Bergen University 59, 1–59.
- Gelchinsky, B., Keydar, S., Helle, H., 1993. Studying of salt dome by homeomorphic technique — a case history. 55th EAEG Conf. and Tech. Exh., Extended Abstracts, PO-64.
- Gelchinsky, B., Hanyga, A., Berkovitch, A., Keydar, S., 1995. Determination of wedge points by high resolution homeomorphic imaging method. 57th EAEG Conf. and Tech. Exh., Extended Abstracts, BO-39.
- Gelchinsky, B., Berkovitch, A., Keydar, S., 2000. Multifocusing homeomorphic imaging: Part 2. Multifold data set and multifocusing, this issue.
- Gelchinsky, B., Berkovitch, A., Keydar, S., 2000. Multifocusing homeomorphic imaging: Part 1. Basic concepts and formulae, this issue.
- Hale, D., 1991. Dip moveout processing. In: Domenico, S.D. (Ed.), *SEG Short Course Notes Series*, Vol. 4. Soc. Exp. Geophys.
- Hubral, P., 1983. Computing true amplitude reflections in a laterally inhomogeneous Earth. *Geophysics* 48, 1051–1062.
- Hubral, P., Krey, T., 1980. Interval velocities from seismic reflection measurements. *SEG*.
- Keydar, S., Gelchinsky, B., Shtivelman, V., Berkovitch, A., 1990. The common evolute element (CEE) stack method (zero-offset stack). 60th Ann. Intern. Mtg., Soc. Exp. Geophys., Expanded Abstracts, pp. 1911–1913.
- Keydar, S., Gelchinsky, B., Berkovitch, A., 1993. The combined homeomorphic stacking method. 63rd Ann. Intern., Soc. Exp. Geophys., Expanded Abstracts, pp. 1141–1144.

- Keydar, S., Edry., Berkovitch, A., Gelchinsky, B., 1995. Construction of kinematic seismic model by homeomorphic imaging method. 57th EAEG Conf. and Tech. Exh., Extended Abstracts, BO-86.
- Keydar, S., Gelchinsky, B., Berkovitch, A., 1996. Common shot point stacking and imaging method. *J. Seismic Explor.* 5, 261–274.
- Keydar, S., Landa, E., Gelchinsky, B., Belfer, I., 1998. Multiple prediction using the homeomorphic imaging technique. *Geophys. Prospect.* 46, 423–440.
- Koren, Z., Gelchinsky, B., 1989. Common reflecting element (CRE) ray tracing for calculation of global multioffset time field. *Geophys. J. Int.* 99, 391–400.
- Levin, F.K., 1971. Apparent velocity from dipping interface reflections. *Geophysics* 36, 510–516.
- Liner, C.L., 1990. General theory and comparative anatomy of dip moveout. *Geophysics* 55, 595–607.
- Mayne, W.H., 1967. Practical considerations in the use of common reflection point technique. *Geophysics* 32, 225–229.
- Notfors, C.D., Godfrey, R.J., 1987. Dip moveout in the frequency–wavenumber domain. *Geophysics* 52, 1708–1721.
- Rabbel, W., Bittner, R., Gelchinsky, B., 1991. Seismic mapping of complex reflectors with common reflecting element (CRE) method. *Phys. Earth Planet. Inter.* 67, 200–210.
- Schleicher, J., Tygel, M., Hubral, P., 1993. 3D true-amplitude finite-offset migration. *Geophysics* 58, 1112–1126.
- Sherwood, J.W.C., Schultz, P.S., Judson, D.R., 1978. Equalizing the stacking velocities of dipping events via Devilish. 48th Ann. Int. SEG Meeting.
- Steentoft, H., Rabbel, W., 1992. The CRE method: a technique of homeomorphic imaging in processing of seismic data. *Acoust. Imaging* 19, 803–809.
- Steentoft, H., Rabbel, W., 1994. Seismic mapping of the Marmousi data set with the common reflecting element method (CRE method). *Tectonophysics* 232, 355–363.
- Tygel, M., Schleicher, J., Hubral, P., 1992. Geometrical-spreading correction of offset reflections in a laterally inhomogeneous Earth. *Geophysics* 57, 1054–1063.
- Wainstein, A., Meshbey, V., Isakov, A., Kessler, D., Gelchinsky, B., 1992. Modeling and studying wavefield scattered by fractal interfaces. 62nd Ann. SEG Meeting, New Orleans, Expanded Abstracts.
- Yilmaz, O., Claerbout, J.F., 1980. Prestack partial migration. *Geophysics* 45, 1753–1777.